Nano-clustering of ligands on surrogate antigen presenting cells modulates T cell membrane adhesion and organization

Pierre Dillard, Fuwei Pi, Annemarie Lellouch, Laurent Limozin, Kheya Sengupta

Nano-clustering of ligands on surrogate Antigen Presenting Cells modulates T cell membrane adhesion and organization

Pierre Dillard[*§†], Fuwei Pi[*†‡], Annemarie C. Lellouch[§], Laurent Limozin[§‖] and Kheya Sengupta [*‖]

We investigate adhesion and molecular organization of the plasma membrane of T lymphocytes interacting with a surrogate antigen presenting cell comprising glass supported ordered arrays of antibody (α-CD3) nano-dots dispersed in a non-adhesive matrix of polyethylene glycol (PEG). The local membrane adhesion and topography, as well as the distribution of the T cell receptors (TCRs) and the kinase ZAP-70, is influenced by dot-geometry, whereas cell spreading area is determined by the overall average density of the ligands rather than specific characteristics of the dots. TCR clusters are recruited preferentially to the nano-dots and the TCR cluster size distribution has a weak dot-size dependence. On the patterns, the clusters are larger, more numerous, and more enriched in TCR, as compared to the homogeneously distributed ligands at comparable concentrations. These observations support the idea that non-ligated TCR residing in the non-adhered parts of the proximal membrane are able to diffuse and enrich the existing clusters at the ligand dots. However, long distance transport is impaired and cluster centralization in form of a central Supramolecular cluster (cSMAC) is not observed. Time-lapse imaging of early cell-surface contacts indicates that the ZAP-70 microclusters are directly recruited to the site of the antibody dots and this process is concomitant with membrane adhesion. These results together point to a complex interplay of adhesion, molecular organization and activation in response to spatially modulated stimulation.

1 Introduction

Many cell membrane proteins are organized in the form of clusters on the membrane (see, for example, recent reviews [1,2], and references therein). Their spatial arrangement and dynamic reorganization play a decisive role in cell adhesion and signaling. In the context of adhesion of tissue forming cells, focal adhesions exemplify the exquisite arrangement and hierarchical binding of proteins in the form of clusters that exhibit considerable dynamics [3,4].

Clustering and reorganization of membrane proteins seems to be ubiquitous [2], and is particularly pertinent for lymphocytes in close contact with antigen presenting cells during the initiation of immune recognition, and the formation of the immunological synapse [5]. In the early stages of T lymphocyte adhesion to an activating surface, T cell receptors (TCR), as well as the integrins $\alpha_L\beta_2$ (LFA-1), are known to form micro-clusters (μ-clusters) at the adhesive interface [1,6–10]. Studies on hybrid T cell/supported lipid bilayer (SLB) systems, where the SLB acts as a surrogate antigen presenting cell (APC) [11], have shown that these clusters are dragged centripetally in an actin dependent manner, [7–9] and finally form the supramolecular activation clusters (SMACs), which themselves span several microns [5,11]. A host of signaling molecules, including the kinase zeta-chain-associated protein kinase 70 (ZAP-70) - one of the first molecules to be recruited to the TCR complex on activation - have been shown to also form μ-clusters [8,12], which may colocalize with the TCR μ-clusters. Recently, the TCR has been shown to be pre-clustered on the membrane in the form of micron or nano scale aggregates [13–15]. Conversely, the natural ligand of TCR, the peptide MHC complex

[*] *Aix-Marseille Université, CNRS, CINaM-UMR 7325, Marseille, 13288, France.*

[§] *Laboratoire Adhésion & Inflammation A ix-Marseille U niversité \ I nserm U 1067 \ CNRS-UMR7333, Marseille 13288, France.*

† These authors contributed equally to this work.

‖ Corresponding authors: sengupta@cinam.univ-mrs.fr, laurent.limozin@inserm.fr

[‡] *Current Address: State Key Laboratory of Food Science and Technology, School of Food Science of Jiangnan University,Wuxi, Jiangsu 214122,China*

(pMHC), is itself clustered on the plasma membrane of antigen presenting cells, prior to contact with T cells[16,17] . Therefore it is highly pertinent to explore the adhesion and spreading of T cells on chemically contrasted substrates presenting micron and sub-micron scale clusters of TCR ligands.

Ever since it was demonstrated that cell survival depends on the size of the adhesion footprint[19], chemically structured surfaces have been used extensively to examine spatial regulation in cell biology[20,21]. Micro-patterning has been used extensively to study tissue cells such as fibroblasts and epithelial cells, with experiments ranging from manipulation of single focal adhesions, to confinement of cells for large throughput screening (see, for example, Piel et al.[22] and references therein). The interaction of hematopoietic cells with patterned substrates have also been studied, though to a lesser extent. Micron scale patterning of TCR ligands has been shown to modulate the structure of the immunological synapse, and the secretion of cytokines[23]. A similar approach used micro-patterning to segregate features containing antibodies against the TCR-complex (α-CD3) and the costimulatory molecule CD28, and showed that optimal T cell activation depends on the specific geometry of the pattern and may depend on the mobility of the Src family kinase Lck within the cell membrane[24]. Patterning was also used for so-called “bait-prey" assays where a micro-pattern of antibodies recruits a membrane protein - the bait (CD4) - which in turn allows the *in situ* study of the recruitment of a prey molecule Lck[25]. Recently, the complementary role of TCR and LFA1 in organizing the actin cytoskeleton was probed by micro-patterning of α-CD3 and ICAM-1 molecules[26]. A very different kind of patterning has been used to create so-called “spatial mutations" in T cells adhering to supported lipid bilayers spatially partitioned into corrals. These experiments have revealed a wealth of information, including the fact that the radial location of TCRs correlates with their signalling capacity[27], and that just two molecules of agonist TCR in a μ-cluster is sufficient to activate a T cell[28].

In tissue cells, nano-patterning of molecules at a scale much smaller than individual focal adhesions has revealed that variations in sub-micron/nano-scale organization impact adhesion and signaling[29,30]. The dependence of the adhesion response on pattern geometry has been related to the size of talin, a cytoplasmic protein that binds the intracellular portion of many integrins and stablises focal adhesions by linking the integrin to the cytoskeleton[31]. The issue of relevant length scale is however still debated for T cells interacting with either pMHC molecules or with α-CD3[32–34].

In the past few years, many different kinds of techniques have been proposed for bio-nanopatterning of surfaces for fundamental studies in cell biology[35]. One of the earliest methods used successfully was dip-pen lithography[36] but its use remains restricted due to the time-consuming nature arising from the need for feature by feature printing that is not fully overcome even by massive parallelization[37]. Creation of chemical contrast by e-beam lithography, which is subsequently used to recruit the relevant proteins, is an option but is limited due to its high cost. A technique that held a lot of promise was nano-contact printing, in imitation of the very popular and successful μ-contact printing, but scaling down is proving to be difficult due to deformation of the stamp. Use of di-block micelle assisted self-assembled gold nano-dots is currently the most successful strategy[29,30]. However, since gold interacts strongly with light, the applicability of gold-based substrates for certain kinds of imaging could, in principle, be restricted.

Colloidal bead lithography has been proposed as an alternative, and has been used either with gold chemistry[38] or with an all-organic approach[39]. The latter metal-free approach is compatible with TIRF and RICM imaging[39,40], and is the technique of choice here. Our implementation has the additional advantage of offering variable pitch and dot-size.

An important aspect of such patterning, that has often been ignored, is the nature of the passive surface in-between the adhesive or activating features. PEG is often used as a repellent and can be thought of as a surrogate glycocalyx. The role of the glycocalyx in cell adhesion is a debated subject[41], but it is clear that cells modulate their adhesive interactions by modulating the density and the thickness of the glycocalyx[42–45]. Here we create patterns of alternating activating and passive zones which can create spatial mutations on T cells at the nano-scale, which are reminiscent of those created with μ-barriers in supported lipid bilayers[27], at the same time allowing “bait-prey" type of assays, for example in the context of ZAP-70 recruitment.

The mechanism and consequence of receptor clustering is an important open question in cell biology in general[46], and for T cell/APC interactions in particular[1,14,47]. While the attention was so far focused on the T cell side, with TCR μ-clusters that are now indisputably recognized as the primary functional signalling unit for T cells and are thought to be pre-clustered on the T cell surface, less attention has been paid to the emerging evidence that the TCR ligands, ie. pMHC molecules, are also pre-clustered on the APC side[16,17,48]. Here we engineer surfaces with controlled clusters of antibodies against the TCR complex, to mimic the presentation of TCR ligands on APCs, and report the consequences for the T-cell arising from such nano-scaled patterning in ligand presentation.

2 Experimental Methods

2.1 Nano-patterning of substrates

A schematic for the entire fabrication process for making the nano-patterned substrates is given in the support information (SI Figure 1).

Ultra-hydrophilic glass coverslides (thickness = 170 $\pm$ 10 μm, Assistent, Karl Hecht KG, Germany) were obtained by cleaning with oxygen plasma (Nanoplas DSB3000-6000 equipped with a SEREN R301 RF power supply, SEREN IPS, USA) at room temperature for 15 min, or by ultrasonication in aqueous solution of a detergent (Hellmanex, Sigma, France), followed by thorough rinsing in ultrapure water (obtained by filtering and reverse osmosis - Elga, UK). Silica colloidal beads with diameters of 4 μm,

This is especially true for peptide-MHC class I. Much less is know about MHC class II[18].

2 μm, or 540 nm and typical poly-dispersity of 10 to 15 % (Polysciences, Inc., Germany) were washed 10 times with ultra-pure water before utilisation. A glass coverslide as prepared above was set at an angle and a pre-calibrated volume of the colloidal suspension was allowed to spread on the slide. Slow evaporation at ambient conditions coupled with strategic change of the angle results in uniform and large area coating with a monolayer of colloidal beads (see also Pi et al.[39]).

Thin films of aluminium (Al) were deposited on the glass coverslides through the colloidal bead mask using a radio-frequency (RF) magnetron sputtering system (modified SMC600 tool by ALCATEL, France) from a mixed Al(99%):Si(1%) target (purity $\geq$ 99.99%, Kurt J. Lesker Company, USA). The geometry of the sputtering system is off-axis and the mean free path is $\sim$10 mm in the operating pressure range. Samples were placed at a distance of 105 mm from the target, on a rotating table (3-5 rpm). After deposition of Al, the primary bead mask was rinsed away by ultra-sonication in ultra-pure water for several seconds, leaving the secondary metal mask (Al-mask) with an array of pits (see also Pi et al.[40]).

2.2 Functionalization

The Al-mask coated slides were placed in a chamber containing (3-Aminopropyl)triethoxysilane (APTES, Sigma, France) in vapor phase, at about 60 °C for one hour. Next, biotin conjugated Bovine Serum Albumin (bBSA, Sigma, France) at a concentration of 20 μg/ml in phosphate buffered saline (PBS, Sigma, France) was incubated on the samples for 30 min. Finally, to remove the sacrificial aluminium mask and reveal the bBSA dots, the coverslide was placed in an alkaline medium at a pH = 11.4 for 2 h at room temperature. If required, the complete removal of Al was verified by optical microscopy. The aluminium free glass slides, containing bBSA dot arrays were thoroughly rinsed with neutral PBS buffer, pH = 7.2. Biotin retained its function in spite of exposure to high pH. At this stage the coverslide was covered with uniform nano-dots of functional bBSA, separated by an expanse of bare glass.

The bare glass separating the bBSA dots was back-filled with a diblock copolymer of poly-L-lysine and poly(ethylene glycol) (PLL-PEG), via incubation in PLL(20)-g(3.5)-PEG(5) copolymer (Susos, Switzerland) dissolved in PBS at a chosen concentration (100 μg/ml for dense layer and 10 μg/ml for sparse layer) for 30 min. The PLL moiety, being positively charged, readily binds to glass, which is negatively charged at neutral pH after cleaning. The PEG moiety remains unbound and discourages further protein binding. The PLL-PEG does not significantly bind to the bBSA dots as verified by using fluorescent PLL-PEG (data not shown). For T-cell adhesion studies, substrates were further functionalized by incubation with 2 μg/ml neutravidin (or neutravidin TexasRed, Invitrogen, USA) for 30 min, followed by incubation in α-CD3 at 2 μg/ml (multibiotinylated UCHT1, Beckman Coulter, France, or for SI Figure 2, monobiotinylated fluorescent labeled OKT3) for 30 min.

Positive controls (c Pos) were prepared as described previously[49], and were in certain cases exposed additionally to appropriate amounts of PLL-PEG (c Pos low and c Pos high). Negative controls were prepared by incubation of appropriate amounts of PLL-PEG on bare glass cleaned as above, and were exposed to appropriate amount of neutravidin and α-CD3 (c Neg low and c Neg high). The characteristics of the five controls are summarized in a table in supporting information. In addition, on negative controls (corresponding to c Neg high or low) with no exposure to α-CD3, cells do not adhere at all.

2.3 Cell culture, fixation and labeling

Jurkat T lymphocytes (Clone E6-1, ATCC, referred hence forth as WT) were cultivated in RPMI 1640 complete medium supplemented with 10% Fetal Bovine Serum (Life Technologies,France) and with 25 mM GlutaMAX (Life Technologies). Cells were in exponential growth phase at the time of activation. The functionalized glass coverslides formed the bottom of a custom made chamber which was filled with HEPES-BSA buffer (20 mM HEPES, pH=7.2, 137 mM NaCl, 5 mM KCl, 0.7 mM Na_2HPO_4, 4 mM D-glucose, 2 mM $MgCl_2$, 1 mM $CaCl_2$, 1% BSA). 250 μl of the medium containing cells was added. The cells were allowed to sediment on to the substrate and were either observed live at 37 °C, or were incubated for 30 min at 37 °C 5% CO_2. Cells were then fixed by incubation in 2% pre-warmed paraformaldehyde for 15 min at 37 °C, followed by extensive rinsing with PBS. The cells were blocked with 1 % BSA overnight and immunostained by incubation with 5 μg/ml of FITC labeled anti-vβ8 (BD Biosciences, USA), which is directed against the beta chain of the T-cell receptor, and/or with Alexa-488 or Rhodamine conjugated phalloidin (Life Technologies, USA) to label filamentous actin, during 60 and 45 min. respectively. Samples were rinsed extensively before imaging. In other experiments two variants of the WT Jurkat cells were employed which stably express either the protein tyrosine kinase ZAP-70 in fusion with GFP (ZAP-GFP) or a membrane anchored GFP (Mem-GFP). ZAP-GFP has been described previously[50]. Mem-GFP was created by amplifying the GFP coding sequencing using a coding primer that encodes the N-terminal 13 amino acids of the murine tyrosine kinase Lck. The amplified product was first captured in to pGEMTZ before cloning into the HindIII/EcoRI sites of pCDNA3.1. The resulting fusion protein, where the Lck sequence is fused to the N-terminus of the GFP, is directed to the cytoplasmic membrane via the myristylation and palmitoylation sites within Lck derived sequence. Wild type E6 Jurkat cell lines were nucleofected with the Amaxa electroporation system using Solution V, program S-018 (Lonza, Basel, Switzerland). Stable transfectants were created by culturing the cells in the presence of 1.2 mg/mL G-418 (Gibco, Carlsbad CA, USA), sorting for GFP positive cells, and cloning by limiting dilution. All clones were evaluated for TCR expression by flow cytometry before use (α-CD3 epsilon clone OKT3, BD Bioscience) and clones with TCR expression levels similar to the WT Jurkat parent line were selected for study.

2.4 Microscopy

Total internal reflection microscopy (TIRFM) and reflection interference contrast microscopy (RICM) were performed using an

inverted microscope (AxioObserver, Zeiss, Goettingen, Germany), equipped with an EM-CCD camera (iXon, Andor, Belfast, North-Ireland). Acquisition was performed using Andor iQ software, Micro-Manager[51] (ImageJ) or ZEN (Zeiss). TIRF and RICM images were taken with a 100X 1.45 NA oil or a custom 100X 1.46 NA oil antiflex objective (Zeiss). For TIRF exposure time was 1 s and fluorescence filter set adapted to Alexa488 or Rhodamine was used. The Atto647 fluorophore was imaged in epifluorescence illumination. To enlarge the field of view, RICM images and time sequences were taken also with a 63x 1.25 NA oil antiflex objective (Zeiss). Exposure time was 100 to 300 ms. Confocal images were taken with a Leica confocal microscope equipped with a 63X, NA 1.4 oil objective.

2.5 Image Analysis

Image analysis was performed using macros written in house in ImageJ/FIJI and IgorPro (Wavemetrics). The nano-dot arrays were analyzed in terms of lattice and motif characteristics. The corresponding patterns formed on the cell membrane were analyzed by first determining the location of each cell as well as the coordinates of the underlying dots, and then using these values as the basis for a dot by dot analysis. *The lattice:* Fast Fourier Transform of the fluorescent image of the pattern in NAV channel provided a qualitative assessment of the lattice ordering. The distribution of dot-pair distance was also calculated based on individual dots position as described below. The location of the first peak of this distribution was taken as the pitch of the lattice. *The motifs:* The dot-motif was assumed to be centro-symmetric and characterized using an automated algorithm in terms of the contrast and full-width at half maximum (FWHM) of the radial profile of fluorescence as performed on individual dots. For this, each dot was detected on the fluorescence image by simple thresholding of the intensity and its location estimated by the position of the center-of-mass of fluorescence intensity. A radial profile was calculated and used to estimate the contrast as defined by $(I_{max} - I_{Min})/(I_{max} + I_{Min})$ and FWHM. For a given experimental condition defining the patterns features, the parameters represented in Figure 1 represent the median of the dot ensemble and the error bar is the median absolute deviation. The values reported in Table 1 are determined manually from intensity profiles of at least 30 dots . Percentage coverage quantifies the proportion of activating surface with respect to the total area, calculated by averaging over an area much larger than the dot-size. All error bars are standard deviations unless otherwise stated.

Cells were analyzed for both global and local properties. *Cell-scale:* Cell adhesion was characterised globally based on the RICM images in terms of adhesion area and membrane roughness. Cell contour was determined from RICM images using a spatial variance filter (applied on a disk of radius 0.64 to 0.8 μm) and thresholding, providing an accurate measurement of the contact area, as previously described[49]. Dark area was determined by intensity thresholding of the segmented RICM image. Additionally, the average of the spatial standard deviation of the RICM intensity (normalized by the background intensity) was reported as a measurement of the membrane roughness. *Dot-scale:* When multidimensional images were available (RICM/dot pattern/fluorescent label of cell), we analyzed the fluorescent label of cell in relation with the underlying dots on the substrate. The center of the dots of the array within the contour of the cell (defined as above from the RICM image), was determined by direct thresholding as above. The centre of each dot was taken as the origin to define a region of interest on the label image and a radial profile. The median image of a dot was built pixel by pixel by taking the median value calculated on all individual dots at each pixel. Contrast and FWHM of the label motif was defined as above.

TCR-clusters: The fluorescent images of TCR were prepared in ImageJ, by first a de-noising step (3X3 median filter), and then segmenting the cells using the corresponding RICM image as described above. An iterative intensity thresholding algorithm was used to segment the clusters. The realization of this algorithm as a plugin written for ImageJ was kindly provided by Dr. Rajat Varma[13]. The algorithm uses an initial intensity threshold (here taken to be the mean intensity under the cell but outside the clusters), an upper cutoff for cluster size (here 4 pixels), a step value for convergence (0.05) and a cutoff value to determine how much to trim each cluster (here 0.8). We verified that the output is robust against small variations in all these parameters. All the parameters were kept constant across samples, except the initial intensity threshold, which was set approximately to the background intensity (excluding TCR clusters) within the cell under consideration. The algorithm outputs the size of the clusters, the number of clusters per cell, and the average intensity in each cluster. This information was directly used to construct the size histograms. The cluster density was calculated by dividing the number of clusters in a cell by the area of the cell as determined from segmentation of RICM image. The average cluster intensity was normalized by the average intensity under the cell to compensate for possible differences in the level of immunostaining. To quantify the centralization of TCR, we defined a cSMAC number as the ratio of the total intensity in the cell and the intensity within a circle of 2 μm centered on the centroid of the intensity distribution (see Dillard et al.[49] for details).

Statistical tests and errors The Student T univariate bilateral test, implemented in R (http://www.r-project.org/) was used to determine significance levels. Throughout, *** signifies $P < 0.001$, ** signifies $P < 0.005$. Error bars are standard deviations unless stated otherwise.

3 Results and Discussion

3.1 Characterisation of the nano-dot array

The protein pattern was created using Nano-sphere Lithography (NL), combined with metal sputtering, followed by sequential functionalization with bio-molecules. The resultant patterns are in the form of antibody nano-dots arranged in a hexagonal array. The distance between the dots (pitch) can be varied by choosing different bead-sizes for the NL and the dot size can be changed by exploiting shadow effects during metal deposition[40]. The dots

Rasband, W.S., ImageJ, U. S. National Institutes of Health, Bethesda, Maryland, USA, http://imagej.nih.gov/ij/, 1997-2014.

comprise a first layer of BSA-biotin to which fluorescent labeled neutravidin (NAV) is bound, which in turn acts as a linker to bind the biotinylated antibody α-CD3ϵ (Figure 1A). The antibody is expected to bind strongly and uniformly to the neutravidin, and we ascertained that indeed it is patterned similarly to the underlying neutravidin dots (SI Figure 2). These composite protein dots are subsequently referred to here simply as dots. The dots are separated by a co-polymer of poly-L-lysine and poly ethylene glycol (PLL-PEG, for simplicity here called the PEG layer). The PLL is bound to the negatively charged glass, and the hydrophilic and uncharged PEG side chains extend into the aqueous phase[52,53]. The dots are imaged in epi-fluorescence (Figure 1) and characterized at the lattice as well as motif level. Table 1 summarizes the various types of patterns, which are named according to their characteristics. B0.5, B2 and B4 signifying pitch of 0.5, 2 and 4 μm respectively, and L, M or S signifying large, medium or small sized dots with 2 μm pitch. The labels "high" or "low" refer to the surface density of PEG.

The regularity of the lattice, which reflects the global arrangement of the dots, can be inferred from the Fourier transform (FFT) of images of the dot-fields. As shown in Figure 1, the FFTs of the dots typically exhibit several diffraction orders showing that spatial ordering is long range. The only exception is B0.5, where the broken ring indicates good positional order but limited orientational order. The dots are further characterized locally by analysis of epi-fluorescence images. To illustrate a "typical" dot, we construct a median image as explained in Methods section. The dot-size expressed as the full width at half maximum (FWHM) does not depend on the surface density of PEG but depends on the parameters set by the fabrication process (Figure 1 and table 1).

Imaging with an atomic force microscope revealed a small difference in layer thickness (about 5 nm) between the two surface concentrations of PLL-PEG (SI Figure 3).

Since the area covered in α-CD3 depends on the dot size and spacing, the overall average ligand-density also varies according to the dot characteristics. For each case, the average ligand-density is slightly lower for high PEG. The ligand-density outside the dots is weakly influenced by the PEG (about 10 $/\mu m^2$ on average). The ligand-density inside the dots is more strongly influenced by the PEG, and varies between about 40 and 60 $/\mu m^2$ for low and between 20 and 45 for high (SI Figure 4).

3.2 Quantification of global cell spreading

Cells from the Jurkat T cell line were allowed to interact with the substrate for thirty minutes, and were then fixed, labeled appropriately, and observed. Due to the slower dynamics of spreading on the patterns, as compared to homogeneously coated substrates[49], the cell is at its peak spread area at thirty minutes. The region of contact between the proximal surface of the cell and the patterned substrate was imaged with reflection interference contrast microscopy (RICM). For the settings used, RICM images those parts of the membrane that are at a distance of at most 2 μm from the surface[54]. This region of proximal cell surface to substrate contact is called the contact zone and the area of this zone, called the contact area, is a measure of cell spreading. Note that in the contact zone the membrane may not be tightly adhered everywhere, but it is in close proximity to the substrate and can potentially interact with it.

The contact area is strongly influenced by the quality of the underlying polymer cushion (Figure 2A). On the layers with low PEG density, the cells consistently spread better than high PEG density case and are more circular. On high PEG density, the cells often exhibit a complex shape. In particular, on the smallest dots (B0.5) the cells spread relatively well but exhibit a very irregular boundary. For the case of 2μm spacing, the cells adhere more as the dot size increases, but the shape remains irregular. Finally, for B4, the contour of the contact area seems to follow the shape of the underlying dots - again resulting in an irregular boundary.

Quantification of the contact area confirms that for each kind of underlying dot-pattern, cells on low PEG density have a larger contact area than those on the layer with high PEG density. Control experiments on surfaces coated with PLL-PEG alone show the same trend (2A, cell area 32 $\pm$ 10 μm^2 for low, compared to 12 $\pm$ 5 μm^2 for high - note that the latter value is exaggerated because many non-adherent cells, with very low area, are washed away during fixation and are not counted in the average). For both cases, the adhesion is significantly lower than on any of the patterns (Figure 2B). For surfaces uniformly coated with the ligand and exposed to the two different PLL-PEG concentrations at the appropriate step during functionalization, the cell adhesion is not appreciably different for the two cases (positive controls in Figure 2).

In case of high PEG surface density, the average molecular density of the ligands on the substrate determines the contact area, which increases monotonically with increasing ligand density (Figure 2C). The average ligand density is primarily determined by the surface coverage and secondarily by the density of the ligands inside the dots (SI Figure 4). The contact area uniquely depends on this average molecular density but does not depend separately on the dot-size or spacing (as also indicated by calculation of Pearson correlation coefficients, SI Figure 5). To verify this hypothesis, we compared the contact area on patterned substrates with control substrates exhibiting an equivalent average molecular density of the ligands, but where molecules are uniformly distributed. Two cases were studied – in the first, the ligands are grafted on a supported lipid bilayer but are immobile; this is expected to fully screen all non-specific interactions. In the second, the ligands are grafted on glass *via* linkers; a residual adhesion (non-zero contact area) in absence of any α-CD3 point to the presence of non-specific interactions[49]. The comparison presented in Figure 2C shows that the *average* ligand-density is in fact the control parameter, when the non-specific interaction is correctly blocked, either by using a supported lipid bilayer, or in the case of patterned substrates, with dense PEG. For sparse PEG, were the non-specific interaction is not fully screened, the correlation between cell spreading and ligand-density is not evident

B0.5 is an exception because the dots are too closely spaced for characterization of size with optical microscopy due to the diffraction limit. In this case, the size was measured by atomic force microscopy imaging, as reported in Pi et al.[40].

(SI Figure 6).

We show above that when the non-specific attraction is fully screened, the extent of spreading is determined by the *average* number of activating molecules per unit area, irrespective of whether they are presented as clusters or are homogeneously distributed. Interestingly, using a combination of pMHC nano and micronanopatterns, it was shown by Deeg et al.[32] and Matic et al.[33] that the total number of ligands encountered by the cell, rather that a local peak ligand-density, determines the proportion of spreading and activating cells, seemingly contradicting previous experiments with corralled SLBs with mobile ligands by Manz et al.[28], which showed that the minimal number of MHC available per TCR, rather than the total amount seen by the cell, determines cell activation. However, contrary to Manz et al., the present study (or that of Deeg/Matic et al.) does not use LFA-1/ICAM-1 bonds to ensure cell adhesion. Instead, the α-CD3 molecules take on a dual adhesive and activating role[6,49,55]. On immobilized ligands the extent of T cell spreading has been shown to be a good indicator of cell activation and proliferation[56], but this is not the case for mobile ligands. The contact area is in fact lowered without affecting the level of activation[49], perhaps since the ligands can gather under the cell, increasing their density locally. Thus our observations confirm the results of Deeg et al[32] that the extent of T-cell activation, here evidenced by its spreading, is determined by average ligand-density when mediated by immobilized ligands.

3.3 Local organization of the membrane

In addition to determining the contact area as above, RICM images also reflect the topography of the proximal membrane since the level of gray in the RICM image is determined by the local distance between the membrane and the surface, typically going from dark to bright and dark again as the distance changes from nearly zero to about hundred nanometer and beyond[54]. In general, darker pixels correspond to tightly adhered membrane. Here, the proximal membrane topography, i.e. the membrane to surface distance, is modulated locally by the dots (Figure 3A). Since the absolute value of the tight adhesion area is influenced by the overall contact area, we normalize the dark area in RICM by the contact area in order to access membrane adhesion independent of cell spreading. This dark area ratio is strongly diminished on high PEG surfaces (SI Figure 7). Overall, for the high PEG surfaces, the ratio shows a clear correlation with the average molecular density of the ligands, but does not show any overall clear dependence on the average ligand-density when the low PEG data are included (SI Figure 8). However, when the low and high PEG data are considered together, a strong correlation between the dark area ratio and the molecular density of the ligands inside the dots is found (see Pearson coefficients in SI Figure 5). The dark area ratio is plotted in Figure 3B as a function of the inside-density and shows a clear dependence. We conclude that the local membrane tight adhesion is determined by the local ligand density.

Another way to quantify the variations in membrane adhesion is through the analysis of membrane roughness, which is an indicator of variations in distance between the T cell membrane and the substrate. The roughness can be considered to be a more robust indicator than calculation of the dark area of tight adhesion since it circumvents possible problems arising from image thresholding[54,57]. We find that the membrane roughness is inversely correlated with ligand-density inside the dots as well as average ligand-density and coverage (Figure 3). The roughness on patterned substrates is always significantly different from the positive controls ($P < 0.001$), as well as between different pitch or dot sizes, and within each type of dot, the roughness depends weakly on the PEG density (Figure 3C). While it is difficult to relate the roughness directly to the properties of the dots, it is clear that for both sparse and dense PEG, the patterns have the ability to modulate the membrane in a specific and pattern dependent manner.

3.4 Local and cell-scale organization of TCR

The distribution of TCR was imaged in TIRF-M (Figure 4) by staining after fixation with an antibody against the β chain of the TCR molecules (anti-Vβ8). Historically, TCR μ-clusters were first identified in live T cells labelled with anti-Vβ8 and interacting with α-CD3 immobilized on glass, as features enriched in TCR molecules which function as signalling assemblies[6] (see also SI Figure 9 and corresponding discussion). Later, using glass supported bilayers carrying mobile ligands, they were shown to undergo actin dependent translocation on the cell membrane without losing their structural cohesion[10] and to eventually centralize to form the cSMAC with the size of several microns[11]. On immobilized ligands (corresponding to our positive control) however, only small clusters are observed even at late times (30 minutes in the present case). In the following discussion, we assume that a local enrichment of TCR, detectable in TIRF microscopy, represents a TCR cluster. It will be seen that on the patterns, in addition to μ-clusters, larger clusters, with size comparable to the cSMAC are also detected.

The cluster characteristics were quantified using an algorithm that identifies them based on an initial intensity threshold followed by iterative segmentation[13]. We report the cluster size distribution, cluster intensity normalized by the average fluorescent intensity under the cell, and cluster density, ie. number per unit area (Figure 4). Visual inspection of the images (Figure 4 and SI Figure 10), show that as expected, Pos has a small population of sub-micron clusters . On B0.5, where the dot size is considerably smaller than the typical TCR μ-cluster size of 1μm[13] reported for mobile TCR-ligands, the TCR cluster distribution is random but larger clusters may be seen. On B2M the TCR-microclusters colocalize with the underlying dots have roughly the same size (see section 3.6 for further size analysis for B2M). The TCR clusters follow the underlying dots so well that the FFT of their images show the underlying hexagonal symmetry (Figure 4A, B2M). Interestingly, in this case, comparison with RICM images show that the TCR clusters are also present in the finger-like structures em-

The α-CD3 present on the pattern targets the ε chain of the CD3 associated with the TCR complex and therefore the two antibodies do not interfere.

anating from the cells. On B4, in addition to sub-micron clusters, very large clusters comparable in size to the underlying dots, and having complex internal organization, are often detected. The TCR clusters are partly localized within the area defined by the underlying dots.

Quantification shows that the number density of clusters (Figure 4B), the maximum cluster size (grey arrow, Figure 4C) and the average intensity within a cluster (Figure 4D) are all greater on the patterns as compared to C Pos, but do not depend on the specific pattern characteristics. Note that the average density of ligands on c Pos (about $40/\mu m^2$) is much higher than the average on the patterns and is comparable to the surface density of ligands inside the dots (about 20-40 $/\mu m^2$, see section 3.1).

Closer inspection of the histogram of size distribution, normalized by cell area and thus representing the density of clusters of each size-bin (SI Figure 10B) shows that the density of all sizes of clusters is least for Pos and highest for B4. Furthermore, the size distribution histogram normalized by the total number of clusters for each case (Figure 4C and SI Figure 10B), shows an increased fraction of clusters in the size range of about 0.6 to 1 μm^2 in 2BM (green arrow) and in the range 3.5 to 4.5 μm^2 for B4 (blue arrow). Few clusters of size 5 to 6 μm^2 is seen on all the patterns but not on c Pos. To summarize, as compared to Pos, on the pattern the clusters are more numerous, larger and the TCR is more concentrated within the clusters; the cluster size weakly depends on the pattern size. These observation can be understood if we recognize that the TCR molecules in the non-adherent parts of the membrane can in fact diffuse around, just like ligated TCRs do on supported lipid bilayers, and eventually enrich existing TCR clusters at the dots. However, we see no evidence that the TCR μ-clusters are gathered into a cSMAC (SI Figure 12). The non-ligated TCR can cluster by diffusion but even after thirty minutes of engagement, we detect no sign of centralization and infer that the non-ligated TCRs are not transported by actin at the cell scale.

3.5 Early dynamics of the cell membrane and ZAP-70 clusters

To compare the results obtained above from cells fixed 30 minutes after engagement with behavior at early times, we followed the spreading dynamics of ZAP-70-GFP and Mem-GFP (a membrane-labeled cell-line) cells while they interacted with surfaces exhibiting B2M dots at low PEG surface density. The cells were allowed to sediment on to the substrate and were imaged in TIRFM. The first contact was visible as punctate structures which form preferentially at the site of the dots. In case of ZAP-70-GFP cells, the puncta mature to ZAP-70 clusters, which are visible at very early times - within about a minute after touch down (Figure 5A and SI movie 1). A maximal projection of a two minutes long sequence (each pixel contains the maximum intensity that it had in the course of the entire sequence) shows that many but not all the dots harbor a ZAP-70 cluster. A closer look at the individual frames reveals that some clusters also disappear within the 2 min observation time. To compare this early localization with the effects arising purely from membrane dynamics, we look at the Mem-GFP cells (Figure 5B and SI movie 2). On B2M with low PEG density, the minimum projection (each pixel contains the minimum intensity that it had in the entire sequence) shows a one-to-one correspondence between the dots and the Mem-GFP. This modulation in the intensity arises because the membrane makes stable contact with the substrate only at the site of the dots - elsewhere, the membrane makes large excursions that take it out of the zone of TIRF illumination, that is more than 200 nm above the substrate. This behaviour is also revealed by the maximal projection and the map of the intensity standard deviation. The fluctuation dynamics of the membrane is even more pronounced in the case of high PEG surface density.

3.6 Dot based analysis of signaling clusters

Having established that the TCR-complex co-localizes with the pattern of its ligands, we looked into the organization of the 70 kD Zeta Associated Protein kinase (ZAP-70) which is one of the first molecules to be recruited by the TCR-complex following activation. Cells expressing ZAP-70-GFP were allowed to spread on B2M, in the same way as the wild type cells above, and were fixed and observed in TIRFM. The co-localization of ZAP-GFP with the dots is less marked than the case of TCR but nevertheless the FFTs show that there is indeed some order induced in the ZAP-70 distribution (Figure 6). Interestingly, the composite image superposing the dots and the ZAP-70 clusters indicates only limited co-localization. This is in fact consistent with the observation in the live imaging that the ZAP-70 clusters engage and dis-engage, because ZAP-70 recruitment to the TCR is a dynamic process.

A quantitative comparison of the TCR and ZAP-70 clusters, in terms of localization of the labeled proteins with the dots, and the cluster size, is presented in Figure 7. The samples were imaged in three channels - the NAV channel to image the dots, the protein label channel to image the TCR/ZAP-70 clusters and the RICM channel to segment the cell. The image of the dots was used to find the coordinates of the antibody nano-dots. The image of the label was first segmented according to the RICM image and then the area under the cell was divided into adjacent non-overlapping square tiles centered on the antibody nano-dots. The tiles are presented in the form of an array (last column in Figure 7). This array representation provides a simple way to assess whether or not a given dot recruits a protein cluster. We used the Mem-GFP cells as control, in order to account for possible bias in TIRFM imaging arising from membrane topography. Adhered Mem-GFP cells, as observed in TIRFM, exhibit large but poorly contrasted patches which are seen to co-localize with the α-CD3 dots (last row in Figure 7A). This effect arises because the membrane exhibits a distinct topography, often adhering closely to the dots but being further from the substrate in the non-adhesive zones, as was already seen from RICM images and in the dynamic data.

In all three cases, there is co-localization of the label (immunostained TCR, ZAP-70-GFP or Mem-GFP) with the underlying dots (Figure 7A). Strikingly there is no apparent correlation between dot intensity and label intensity (SI Figure 13). There is also no obvious influence of the quality of the polymer cushion. The Mem-GFP dots, as well as the ZAP-70 dots are poorly contrasted whereas both the TCR clusters achieve at least 40% contrast (Fig-

ure 7B). The Mem-GFP dots are however, marginally larger in size than the TCR and the ZAP-70 clusters (Figure 7C), but all of these are smaller than the expected size of the dots, which is about 700 nm. A cumulative histogram of the contrast (Figure 7D) shows that while the contrast for the case of ZAP-70 with high PEG density is indistinguishable from the contrast of Mem-GFP, and is hence likely to arise from the combination of topography and TIRF effect as discussed above, the contrast for ZAP-70 with low PEG density, as well as both TCR cases, is distinct from that of the Mem-GFP and points to real clustering.

4 Conclusion

Here we showed that the cells are able to sense a chemical contrast on the substrate, presented in the form of dots with elevated levels of α-CD3 inside and PEG polymer chains outside. This sensing is at a local level – the cells reorganize the molecular distribution of TCR and ZAP-70 as well as the topography of their membrane in response. Interestingly, the cell spreading response, at the global cell scale, depends not on the local α-CD3 distribution but on the overall ligand density - the cells integrate the submicron signal and respond to the average. We established that the repulsive polymer layer not only prevents non-specific adhesive interaction of the cell membrane with the glass but also acts as a reservoir for unligated diffusive TCR, with the consequence that on the patterned substrates the TCR clusters are brighter and more numerous. The diffusive TCR is however not coupled to the actin retrograde flow, evidenced by the lack of centralization seen with mobile ligands on supported lipid bilayers[49]. Interestingly, while the spreading response is strongly dependent on the quality of the PEG layer - cell spread more on less dense PEG layer and also fail to show any correspondence between ligand density and area - the membrane organization, both in terms of area of tight contact and assembly of TCR, is independent of PEG density.

We used novel substrates exhibiting chemically contrasted nano-dot patterns to probe T cell adhesion. A crucial improvement here with respect to previous work is the diminution of pitch and dot size. Since the typical size of a spread T cell[49] is about 300 μm^2, it is essential to use sub-micron scale patterns in order to get a reasonable number of dots under a cell. In contrast to previous work where large micrometric size severely limited certain applications (e.g. large surrogate transfected cells rather than real T cells were used[25]), sub-micron scales could be achieved here. At nano-scale[32–34] the emphasis previously was on achieving single-molecule islands, necessitating the use of gold nanoparticles that scatter light and limit surface sensitive advanced imaging. The novel substrates used here, being fully compatible with RICM and TIRFM, allowed us to develop non-standard, and automated analysis protocols. These include exploitation of FFTs to infer ordering in a quick and robust manner, and quantification of localization on a dot-by-dot basis leading to fast accumulation of data for hundreds of dots.

During cell adhesion, the proximal membrane flattens and forms a more-or-less homogeneous contact with the substrate. This zone of contact is however not perfectly flat (see for example electron microscopy image of T cell/APC interface[58]) since regions of close contact coexist with zones with a distinct gap between the membranes. One of the consequences is that small, but not large molecules can pass in and out of the contact zone[59]. Our patterning technology has permitted us to mimic such a partial adhesion scenario, and has shed light on the different roles that glycocalyx rich zones may play in T cell/APC interactions. On one hand, the presence of glycocalyx can modulate adhesion (Figure 2), perhaps in analogy with model membranes[60,61], and on the other hand glycocalyx rich non-adhered patches act as reservoir for non-ligated TCR which seem to have a weakened or non-existent coupling to actin (Figure 4 and SI Figure 12).

The membrane topography, generated here with the help of the repulsive zones, may be particularly important in T cells since it may play a role in regulating T-cell activation, as hypothesized in the kinetic-segregation model, where CD45 or CD148 phosphatases with long extracellular domains are excluded from zones of close T cell - APC membrane apposition mediated by the short and clustered TCR-MHC bonds[42,62]. Whether initially the clustering occurs due to lateral interactions or an active mechanism[63] is debatable but our experiments show that clustering of pMHC on the APC surface is likely to influence segregation on the T cell surface. It can be speculated that in analogy with the case of mucins around focal adhesions[45], the presence of long molecules may improve TCR signaling.

The formation of inhomogeneous membrane topography is closely linked to TCR clustering, which is believed to be crucial for T cell signaling[1,8]. Recent work indicates that TCR are preclustered as nano or micro domains which mature upon ligation of TCR[13–15,64]. The focus in the literature has been on the case where the ligands (pMHC or α-CD3) are mobile. However, μ-clusters may also form on immobilized ligands[6,12]. In both cases, on substrates with homogeneous distribution of ligands, the TCR μ-clusters are randomly distributed[6,10,13], as is reproduced in our positive controls. The substrates used here present a third possibility - on the dots, the TCR is expected to be immobilized upon ligation, whereas on the passive PEG covered zones, the TCRs, presumably unligated and present either as monomers or in preclustered form, should be fully mobile. This allows freely diffusing, unligated TCRs to diffuse onto the activating dots and to reinforce the clusters already immobilized at these sites. In contrast, on fixed ligands, all the TCR are bound and immobilized soon after cell spreading, thus preventing maturation of TCR clusters (Figure 4). A typical size of about 1μm has been reported for TCR μ-clusters formed on mobile ligands[13]. Interestingly, using gold nano particle arrays as a sieve[65], it was shown that the size of TCR μ-clusters probably reduce with ligand-density, reaching down to 80 nm for an effective agonist peptide average density of 4/μm^2. Here, working with a range of average ligand density of about 10 to 30 /μm^2, we did not detect any size dependence on density or a favoured size, instead the cluster size weakly reflects the dot-size (Figure 4). This should be interpreted in the light of the fact that here the ligated TCRs are not mobile, where as in the sieve experiment, they remain mobile on ligation. The scenario

cited values are for Jurkat cell line used here, primary T cells are even smaller.

Table 1 Characteristics of the patterned protein nano-dot arrays.

Acronym	Pitch (μm)	Dot size (μm)	Coverage (percent)	Density (per μm^2)
B4 high	4	1.6 ± 0.1	18 ± 1	15 ± 4.2
B4 low		1.6 ± 0.1		22 ± 4.5
B2L high	2	0.98 ± 0.1	22 ± 2	18 ± 5.3
B2L low		0.98 ± 0.1		25 ± 5.1
B2M high	2	0.64 ± 0.03	11 ± 1	12 ± 3.8
B2M low		0.67 ± 0.05		16 ± 3.9
B2S high	2	0.5 ± 0.1	7 ± 1	8 ± 1.6
B2S low		0.5 ± 0.1		12 ± 2.2
B0.5 high	0.5	0.3	32	27 ± 3.5
Pos	N.A	N.A	100	43.5 ± 5

The patterns are named according to their characteristics. B0.5, B2 and B4 signifying pitch (spacing) of 0.5, 2 and 4 μm respectively. B2L, B2M and B2S refer to large, medium and small sized dots with spacing of 2 μm. The labels "high" or "low" refer to the surface density of PEG. Pos is positive control with uniform protein distribution. The dot size reported are full width at half maximum (FWHM) measured from three to ten frames of epi-fluoresce images, each containing hundreds of dots. The percentage coverage quantifies the proportion of activating surface with respect to the total area. The ligand density (averaged over an area much larger than the dot-size) is determined from quantification of images with fluorescent neutravidin. Errors are standard deviations.

presented here is consistent with the idea of TCR pre-clustering. Note that it is difficult to observe pre-clustering directly in TIRF-M since adhesion[66] or mechanical stimulations[67] can cause the cell to be activated and therefore start forming clusters.

The late time centralization of TCR into the central supramolecular activation cluster (cSMAC) is actin driven[10,68], and it has been hypothesized that the TCRs (and integrins) are connected to actin through a frictional coupling[49,69]. Based on the fact that we see no centralization of the free TCR (SI Figure 12), we predict that this frictional coupling to actin is different for ligated or non-ligated TCR, an effect that was already predicted for LFA-1[49].

ZAP-70 is one of the first molecules to be recruited to the TCR complex upon ligation, and its recruitment has been taken as an indicator of TCR triggering[70]. Here, early contacts show frequent ZAP-70 clusters on top of the dots, supporting the idea of preformed TCR-CD3-ZAP70 complexes[71] (Figure 5). However, at later times, colocalization of ZAP-70 with dots is poor. This is compatible with a rapid recruitment of ZAP-70 by CD3, followed by a release of the kinase by the receptor complex[70]. Intriguingly, a FFT signal is still measurable at late times (Figure 7), indicating that ZAP-70 conserves a global organization imposed by the dots. This points to complex dynamics between the TCR-CD3 complex and ZAP-70[47], which may involve both the kinase activity and the adaptator protein function of ZAP-70[72].

The above discussion shows that at a *local scale*, the presentation of the ligands as nano-clusters has an impact on organization of the cell surface molecules and membrane configuration. At the *scale of the cell* however, the response, as measured from cell spreading, is independent of the specific nature of clustering and depends only on the *average* density of ligands. Using gold nano-dots as support, and different measures of activation like IL2 production or proliferation, both Matic et al.[33] and Deeg et al[32] also concluded that overall activation depends on average, rather than local, densities. However, in their case, the local impact could not be probed due to the small size of the gold nano-dots.

We clearly demonstrate a dual scale of T cell response to subcellular patterns — locally, the cell responds at the nano-scale and restructures its molecular distribution; globally, it integrates the signal and responds to an average dose. The results presented here emphasize the need to integrate a hitherto overlooked aspect of APC membranes, namely presentation of ligands in the form of clusters, in design of surrogate APCs.

Acknowledgements

We thank Pierre-Henri Puech, Anne Pierres, Pierre Bongrand and Rajat Varma for insightful discussions, Rajat Varma for sharing analysis code and kind gift of labelled α-CD3, and for critical reading of the manuscript. KS and FP thank Anne Charrier for expert guidance with AFM, and Igor Ozerov for help with sputtering. Nanofabrication was done at PLANETE clean-room facility. LL thanks the Labex Inform for providing a stimulating discussion forum. This work was partially funded by ANR-09-JCJC-0091 DissecTion and by European Research Council via grant no. 307104 FP/2007-2013/ERC-Stg SYNINTER.

References

1 M. Dustin and J. Groves, *Annual Review of Biophysics*, 2012, **41**, 543–556.

2 C. Schuberth and R. Wedlich-Soeldner, *Biochimica et Biophysica Acta-Molecular Cell Research*, 2015, **1853**, 767–774.

3 A. Bershadsky, M. Kozlov and B. Geiger, *Current Opinion in Cell Biology*, 2006, **18**, 472–481.

4 C.-h. Yu, N. Rafiq, A. Krishnasamy, K. Hartman, G. Jones, A. Bershadsky and M. Sheetz, *Cell Reports*, 2013, **5**, 1456–1468.

5 C. R. Monks, B. A. Freiberg, H. Kupfer, N. Sciaky and A. Kupfer, *Nature*, 1998, **395**, 82–86.

6 S. C. Bunnell, D. I. Hong, J. R. Kardon, T. Yamazaki, C. J. McGlade, V. A. Barr and L. E. Samelson, *J Cell Biol*, 2002, **158**, 1263–1275.

7 G. Campi, R. Varma, and M. L. Dustin, *The Journal of Experimental Medicine*, 2005, **202**, 1031–1036.

8 T. Yokosuka, K. Sakata-Sogawa, W. Kobayashi, M. Hiroshima, A. Hashimoto-Tane, M. Tokunaga, M. L. Dustin and T. Saito, *Nat Immunol*, 2005, **6**, 1253–1262.

9 R. Varma, G. Campi, T. Yokosuka, T. Saito and D. M.L., *Immunity*, 2006, **25**, 117–127.

10 Y. Kaizuka, A. D. Douglass, R. Varma, D. M.L. and R. D. Vale, *Proc Natl Acad Sci U S A*, 2007, **104**, 2029620301.

11 A. Grakoui, S. K. Bromley, C. Sumen, M. M. Davis, A. S. Shaw, P. M. Allen and D. M.L., *Science*, 1999, **285**, 221227.

12 S. C. Bunnell, *Immunological Synapse*, Springer, 2010, pp. 123–154.

13 T. J. Crites, K. Padhan, J. Muller, M. Krogsgaard, P. R. Gudla, S. J. Lockett and R. Varma, *J Immunol*, 2014, **193**, 56–67.

14 K. Beck-Garcia, E. Beck-Garcia, S. Bohler, C. Zorzin, E. Sez-

gin, I. Levental, B. Alarcon and W. W. A. Schamel, *Biochimica et Biophysica Acta-Molecular Cell Research*, 2015, **1853**, 802–809.

15 K.-H. Roh, B. F. Lillemeier, F. Wang and M. M. Davis, *Proceedings of the National Academy of Sciences of the United States of America*, 2015, **112**, E1604–E1613.

16 X. Lu, J. S. Gibbs, H. D. Hickman, A. David, B. P. Dolan, Y. Jin, D. M. Kranz, J. R. Bennink, J. W. Yewdell and R. Varma, *Proc Natl Acad Sci U S A*, 2012, **109**, 15407–15412.

17 M. Ferez, M. Castro, B. Alarcon and H. M. van Santen, *The Journal of Immunology*, 2014, **192**, 52–58.

18 D. R. Fooksman, *Frontiers in Immunology*, 2014, **5**, 158.

19 C. Chen, M. Mrksich, S. Huang, G. Whitesides and D. Ingber, *Science*, 1997, **276**, 1425–1428.

20 M. Wu, D. Holowka, H. Craighead and B. Baird, *Proc Natl Acad Sci U S A*, 2004, **101**, 13798–13803.

21 A. Singhai, D. Wakefield, K. Bryant, S. Hammes, D. Holowka and B. Baird, *Biophys. J.*, 2014, **107**, 2639–2651.

22 M. Piel and M. Thery, *Micropatterning in cell biology, Part B*, Elsevier Academic Press Inc, San Diego, USA, 2014, vol. 120, pp. XV–XVI.

23 J. Doh and D. J. Irvine, *Proc Natl Acad Sci U S A*, 2006, **103**, 5700–5705.

24 K. Shen, V. K. Thomas, M. L. Dustin and L. C. Kam, *Proc Natl Acad Sci U S A*, 2008, **105**, 7791–7796.

25 M. Schwarzenbacher, M. Kaltenbrunner, M. Brameshuber, C. Hesch, W. Paster, J. Weghuber, B. Heise, A. Sonnleitner, H. Stockinger and G. J. Schütz, *Nat Methods*, 2008, **5**, 1053–1060.

26 E. Tabdanov, S. Gondarenko, S. Kumari, A. Liapis, M. L. Dustin, M. P. Sheetz, L. C. Kam and T. Iskratsch, *Integr Biol (Camb)*, 2015, **7**, 1272–1284.

27 K. D. Mossman, G. Campi, J. T. Groves and M. L. Dustin, *Science*, 2005, **310**, 1191–1193.

28 B. N. Manz, B. L. Jackson, R. S. Petit, M. L. Dustin and J. Groves, *Proc Natl Acad Sci U S A*, 2011, **108**, 9089–9094.

29 J. P. Spatz and B. Geiger, *Methods Cell Biol*, 2007, **83**, 89–111.

30 J. Huang, S. V. Grater, F. Corbellini, S. Rinck, E. Bock, R. Kemkemer, H. Kessler, J. Ding and J. P. Spatz, *Nano Lett*, 2009, **9**, 1111–1116.

31 M. Schvartzman, M. Palma, J. Sable, J. Abramson, X. Hu, M. P. Sheetz and S. J. Wind, *Nano Lett*, 2011, **11**, 1306–1312.

32 J. Deeg, M. Axmann, J. Matic, A. Liapis, D. Depoil, J. Afrose, S. Curado, M. L. Dustin and J. P. Spatz, *Nano Lett*, 2013, **13**, 5619–5626.

33 J. Matic, J. Deeg, A. Scheffold, I. Goldstein and J. P. Spatz, *Nano Lett*, 2013, **13**, 5090–5097.

34 D. Delcassian, D. Depoil, D. Rudnicka, M. Liu, D. M. Davis, M. L. Dustin and I. E. Dunlop, *Nano Lett*, 2013, **13**, 5608–5614.

35 S. T. Kim, M. Touma, K. Takeuchi, Z.-Y. J. Sun, V. P. Dave, D. J. Kappes, G. Wagner and E. L. Reinherz, *J Immunol*, 2010, **185**, 2951–2959.

36 Piner, Zhu, Xu, Hong and Mirkin, *Science*, 1999, **283**, 661–663.

37 K. Salaita, Y. Wang, J. Fragala, R. A. Vega, C. Liu and C. A. Mirkin, *Angew Chem Int Ed Engl*, 2006, **45**, 7220–7223.

38 S. H. Kristensen, G. A. Pedersen, L. N. Nejsum and D. S. Sutherland, *Nano Lett*, 2012, **12**, 2129–2133.

39 F. Pi, P. Dillard, L. Limozin, A. Charrier and K. Sengupta, *Nano Lett*, 2013, **13**, 3372–3378.

40 F. Pi, P. Dillard, R. Alameddine, E. Benard, A. Wahl, I. Ozerov, A. Charrier, L. Limozin and K. Sengupta, *Nano letters*, 2015, **15**, 5178–5184.

41 P. Robert, L. Limozin, A.-M. Benoliel, A. Pierres and P. Bongrand, in *Principles of cellular engineering: Understanding the biomolecular interface*, ed. M. King, Elsevier Academic Press, 2006, ch. Glycocalyx regulation of cell adhesion, pp. 143–169.

42 K. Choudhuri, D. Wiseman, M. H. Brown, K. Gould and P. A. van der Merwe, *Nature*, 2005, **436**, 578–582.

43 S. Sabri, M. Soler, C. Foa, A. Pierres, A. Benoliel and P. Bongrand, *J Cell Sci*, 2000, **113 (Pt 9)**, 1589–1600.

44 K. D. Patel, M. U. Nollert and R. P. McEver, *J Cell Biol*, 1995, **131**, 1893–1902.

45 M. J. Paszek, C. C. DuFort, O. Rossier, R. Bainer, J. K. Mouw, K. Godula, J. E. Hudak, J. N. Lakins, A. C. Wijekoon, L. Cassereau, M. G. Rubashkin, M. J. Magbanua, K. S. Thorn, M. W. Davidson, H. S. Rugo, J. W. Park, D. A. Hammer, G. Giannone, C. R. Bertozzi and V. M. Weaver, *Nature*, 2014, **511**, 319–325.

46 B. Alarcon, M. Reth and W. Schamel, *Biochimica et Biophysica Acta (BBA) - Molecular Cell Research*, 2015, **1853**, 765 – 766.

47 Y. Neve-Oz, Y. Razvag, J. Sajman and E. Sherman, *Biochim Biophys Acta*, 2015, **1853**, 810–821.

48 B. Bosch, E. L. Heipertz, J. R. Drake and P. A. Roche, *Journal of Biological Chemistry*, 2013, **288**, 13236–13242.

49 P. Dillard, R. Varma, K. Sengupta and L. Limozin, *Biophys J*, 2014, **107**, 2629–2638.

50 R. Evans, A. C. Lellouch, L. Svensson, A. McDowall and N. Hogg, *Blood*, 2011, **117**, 3331–3342.

51 A. Edelstein, N. Amodaj, K. Hoover, R. Vale and N. Stuurman, *Current protocols in molecular biology*, 2010, 14–20.

52 D. L. Elbert and J. A. Hubbell, *Chemistry & biology*, 1998, **5**, 177–183.

53 G. L. Kenausis, J. Vörös, D. L. Elbert, N. Huang, R. Hofer, L. Ruiz-Taylor, M. Textor, J. A. Hubbell and N. D. Spencer, *The Journal of Physical Chemistry B*, 2000, **104**, 3298–3309.

54 L. Limozin and K. Sengupta, *Chemphyschem*, 2009, **10**, 2752–2768.

55 C.-J. Hsu, W.-T. Hsieh, A. Waldman, F. Clarke, E. S. Huseby, J. K. Burkhardt and T. Baumgart, *PloS one*, 2012, **7**, e32398.

56 E. Cretel, D. Touchard, P. Bongrand and A. Pierres, *J Immunol Methods*, 2011, **364**, 33–39.

57 K. Sengupta, H. Aranda-Espinoza, L. Smith, P. Janmey and D. Hammer, *Biophysical Journal*, 2006, **91**, 4638–4648.

58 K. Choudhuri, J. Llodrá, E. W. Roth, J. Tsai, S. Gordo, K. W. Wucherpfennig, L. C. Kam, D. L. Stokes and M. L. Dustin,

Nature, 2014, **507**, 118–123.

59 A. N. R. Cartwright, J. Griggs and D. M. Davis, *Nat Commun*, 2014, **5**, 5479.

60 L. Limozin and K. Sengupta, *Biophys J*, 2007, **93**, 3300–3313.

61 K. Sengupta and L. Limozin, *Phys Rev Lett*, 2010, **104**, 088101.

62 S.-P. Cordoba, K. Choudhuri, H. Zhang, M. Bridge, A. B. Basat, M. L. Dustin and P. A. van der Merwe, *Blood*, 2013, **121**, 4295–4302.

63 F. Baumgart and G. J. Schütz, *Biochim Biophys Acta*, 2015, **1853**, 791–801.

64 W. W. A. Schamel and B. Alarcón, *Immunol Rev*, 2013, **251**, 13–20.

65 N. G. Caculitan, H. Kai, E. Y. Liu, N. Fay, Y. Yu, T. LohmuÌĹller, G. P. OâĂŹDonoghue and J. T. Groves, *Nano letters*, 2014, **14**, 2293–2298.

66 R. A. Fernandes, J. Huo, Y. Lui, J. H. Felce and S. J. Davis, *Frontiers in immunology*, 2012, **3**, 1–4.

67 S. Cazaux, A. Sadoun, M. Pélicot-Biarnes, M. Martinez, S. Obeid, P. Bongrand, L. Limozin and P.-H. Puech, *Ultramicroscopy*, 2016, **160**, 168–181.

68 P. Beemiller, J. Jacobelli and M. F. Krummel, *Nature immunology*, 2012, **13**, 787–795.

69 N. C. Hartman, J. A. Nyeb and J. T. Groves, *Proceedings of the National Academy of Sciences of the United States of America*, 2009, **106**, 12729–12734.

70 G. P. ODonoghue, R. M. Pielak, A. A. Smoligovets, J. J. Lin and J. T. Groves, *Elife*, 2013, **2**, e00778.

71 B. Malissen and P. Bongrand, *Annu Rev Immunol*, 2015, **33**, 539–561.

72 M. R. Jenkins, J. C. Stinchcombe, B. B. Au-Yeung, Y. Asano, A. T. Ritter, A. Weiss and G. M. Griffiths, *Elife*, 2014, **3**, e01310.

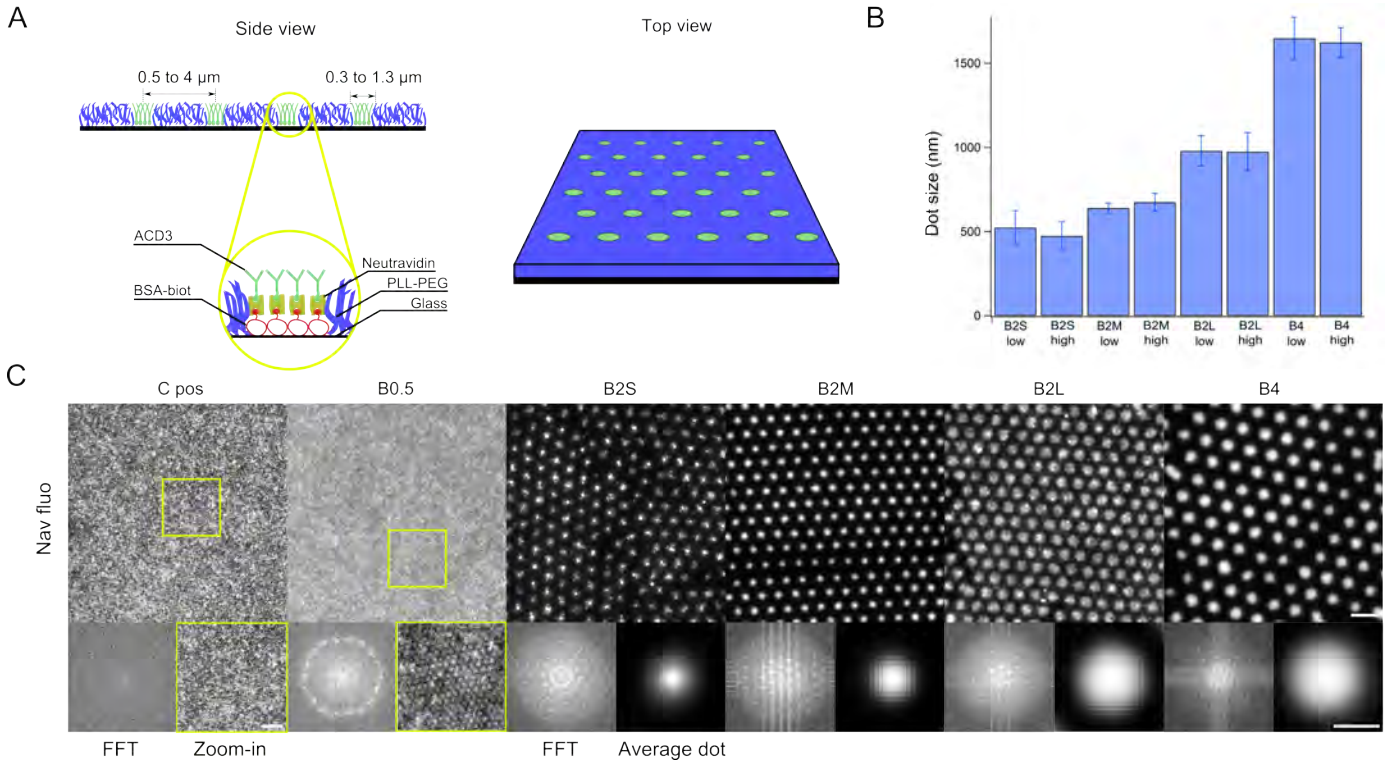

Fig. 1 The substrates. (A) A schematic representation of the patterned substrate (not to scale). (B) Quantification of the size of the antibody nano-dots from fluorescence images of the underling neutravidin. The full width at half maximum (FWHM) of a median dot is reported. A “median dot" is created for each image field, typically containing hundreds of dots and its FWHM is determined. The FWHM is then averaged for at least ten fields for a given case. The error-bars are median absolute deviation. B2S, B2M, B2L and B4 refer respectively to dots with 2 or 4 μm spacing and small, medium or large size; high or low refers to PEG surface density. The dot-size does not depend on PEG density but is set by the choice of parameters during the fabrication process. (C) Epi-fluorescence images of the dots corresponding to each spacing and size, shown for the case of high PEG surface density. The data for low PEG density is equivalent. Scale bars: upper row: 5 μm; lower row: 1μm.

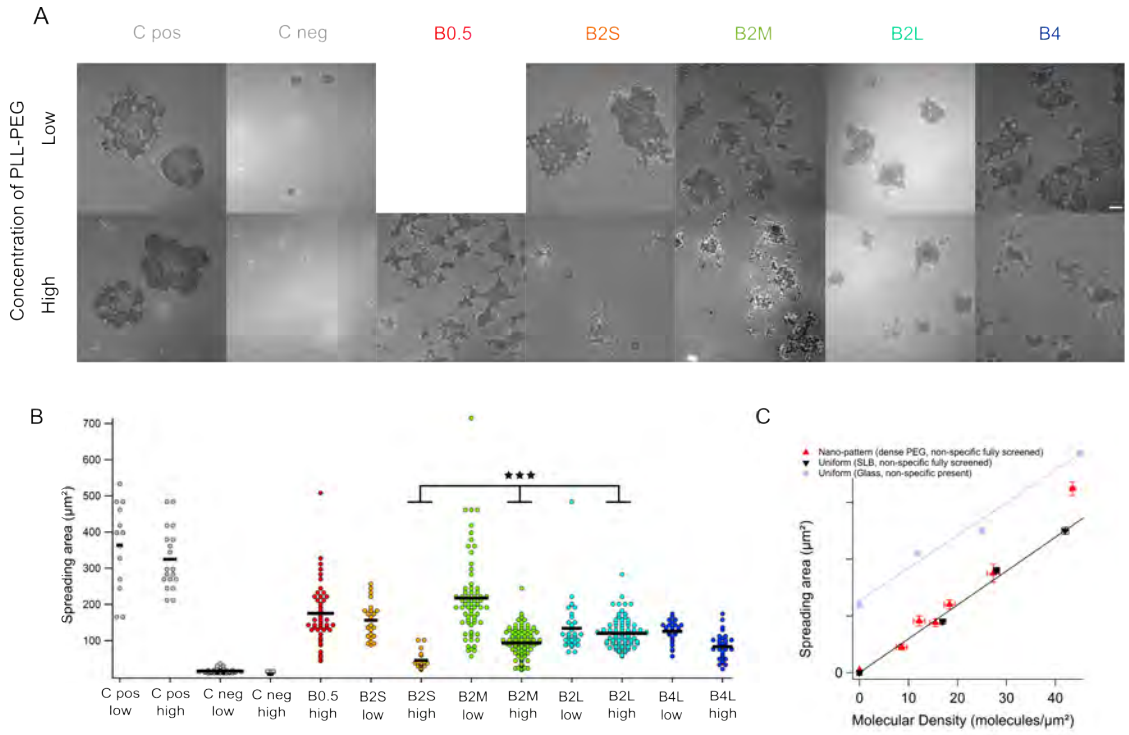

Fig. 2 The cell-surface contact area as determined from segmentation of Reflection Interference Contrast Microscopy (RICM) images. (A) Examples of RICM of cells on the different substrates after 30 minutes of spreading. C Pos are positive controls with uniformly coated α-CD3 exposed further to PLL-PEG, C Neg are negative controls, where in case of high PEG surface density, the non-specific interaction with glass is fully screened and the cells do not adhere at all, whereas for layers with low PEG density, there is residual adhesion. On patterned substrate, the contact area depends on the PEG surface density such that cells spread more on low PEG density surfaces. On C Pos, the PEG density does not significantly impact the cell surface contact. Scale bar 5 μm. (B) Scatter-dot plot of contact area calculated from RICM images; At least 20 cells in each case. Bar = median value. *** : $P < 0.001$. (C) The contact area as a function of average molecular density of the ligands for the patterned substrates (red data) in case of high PEG coverage, and for supported lipid bilayer homogeneously covered surface with immobilized α-CD3 (black data and linear fit). The unspecific interaction is screened in both cases and the cell area is determined only by the average molecular densities. Control substrates with α-CD3 immobilized on glass show similar trend but have an additional contribution from non-specific interactions (blue-gray data and linear fit). Error bars are standard errors.

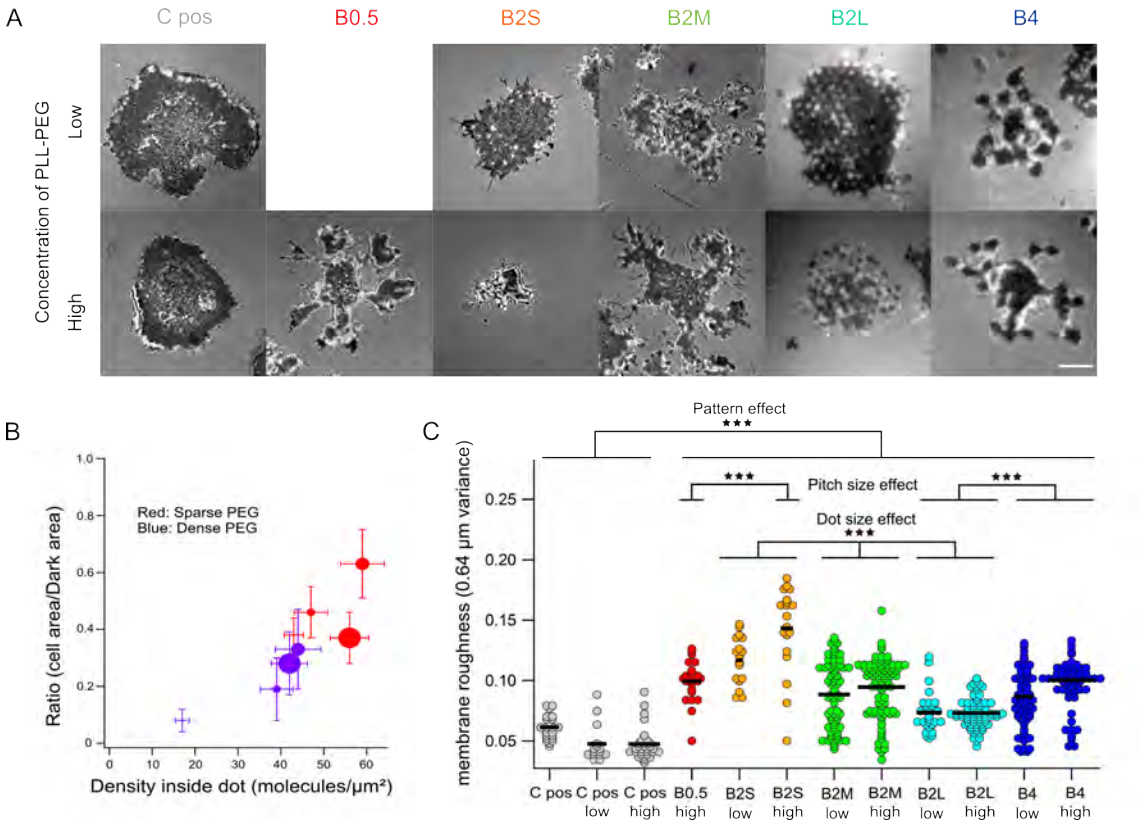

Fig. 3 Membrane topography from RICM images of cells on different patterns. (A) Selected examples that clearly exhibit modulation in RICM signal under the cell indicating that the membrane topography is spatially modulated. Scale bar 5 μm. (B) The ratio of the contact area to tight adhesion area, plotted against the average ligand-density inside the dots for the different patterns, both high and low PEG cases follow a trend. The symbol size reflects the dots size (from large to small: 4B,2BL,2BM and 2BS). Error bars are standard deviations. (C) Scatter dot plots of membrane roughness parameter calculated from the RICM images (at least 20 cells each). For all the patterns, the roughness is substantially higher than on the positive controls (C pos, C pos low and C pos high), corresponding to uniformly coated α-CD3 that is either used as is or after exposure to conditions corresponding to low or high PEG density. On the pattern, for a given dot characteristic, the roughness is usually higher on the high PEG density case. For a given PEG density, the roughness is statistically different for the different dot characteristics. *** : $P < 0.001$.

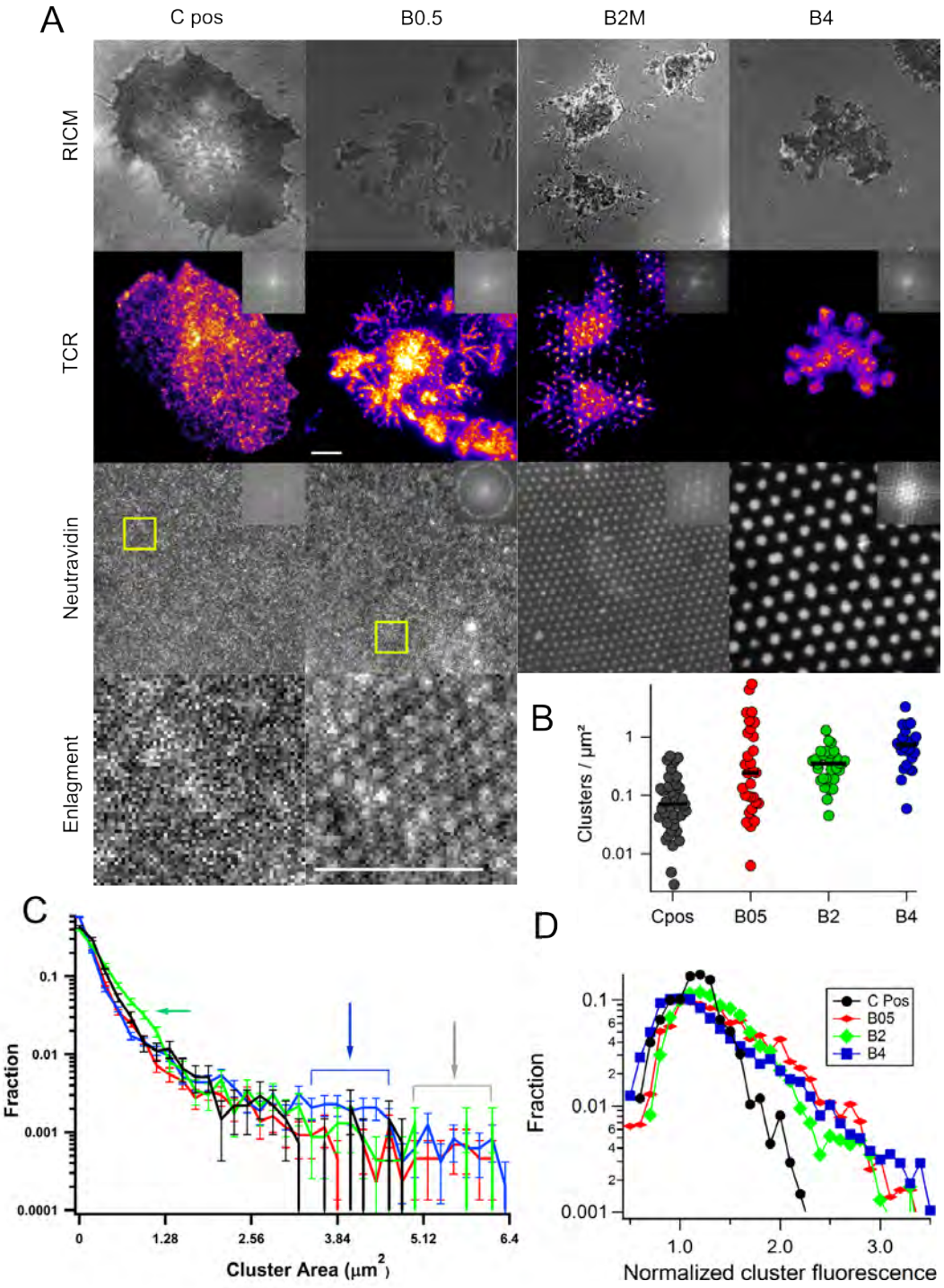

Fig. 4 Distribution of T cell receptors (TCR). Cells were allowed to interact with dots (size as indicated, high PEG density), were fixed and labeled with a fluorescent antibody against the TCR. (A) Top row: RICM images, middle row: TIRFM images of the marked cells in pseudo-colour to emphasise the differences in local concentration of the TCR, bottom row: underlying antibody dots, the fluorescent neutravidin is imaged. Column 1: positive control with randomly distributed TCR clusters. Column 2: On B0.5 cells exhibit many peripheral projections, clearly visible in the TCR channel but the TCR clusters are not visibly different from pos. Column 3: On B2M, the TCR clusters are clearly visible and are usually well localized on the site of the underlying antibody dots as evidenced by FFT in inset. Column 4. On B4, the TCR clusters are usually localized on the dots but a closer inspection shows that each dot often recruits several clusters. Insets show FFT which reflects the ordering (or not) of the TCR clusters. Scale bar 5 μm. (B) Scatter dot plot of the number of clusters per μm^2. Densities are lower for C Pos (black) and comparable for the three patterned substrates (B0.5 red,B2M green,B4 blue). (C) Histogram of apparent area of clusters normalized by the total number of clusters. Clusters of certain size are enriched for B2M (green arrow) and B4 (blue arrow). All the patterns have a small population of very large clusters that do not appear on Pos (grey arrow). (D) Histogram of cluster mean fluorescence (normalized by average intensity under a cell). Intensities (and hence TCR concentration) are lower for C Pos and comparable for the three patterned substrates. Note that the average ligand concentration for C Pos is much higher than the average for the patterned substrates and is in fact comparable to the density inside the dots.

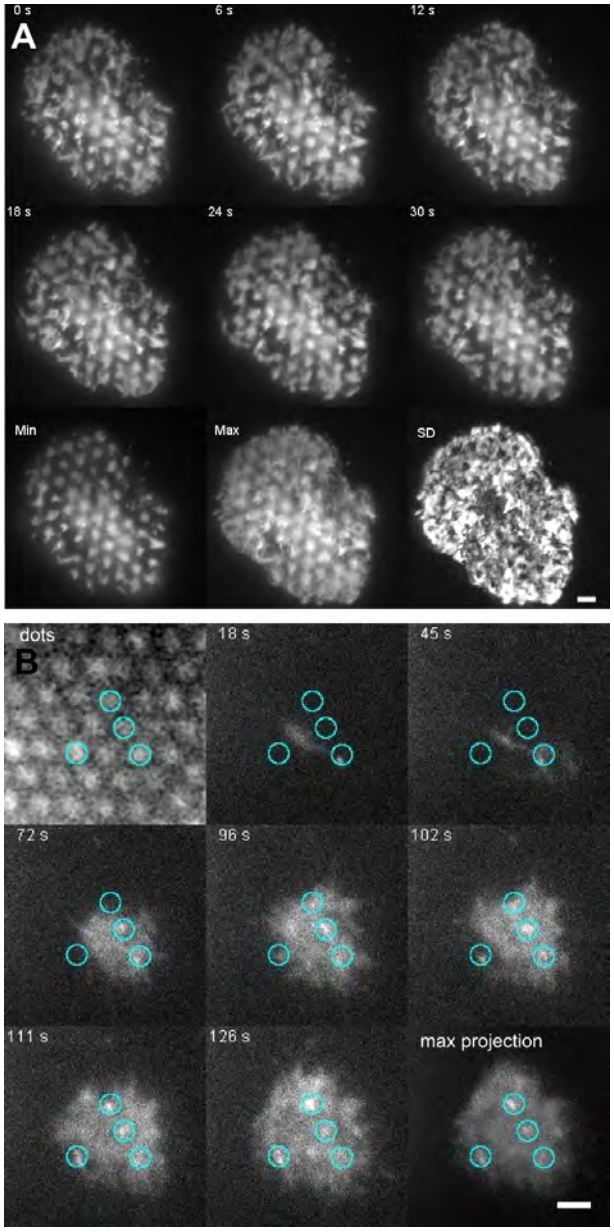

Fig. 5 Live-cell imaging with ZAP-70-GFP and Mem-GFP cells. Zap-70-GFP or Mem-GFP cells were deposited on patterned substrates (B2M, low PEG) and were observed in time-lapse TIRFM. (A) Mem-GFP cells, observed after ca. 5 min., the dynamics of adhesion is described by the time projection (pixel by pixel statistics as a function of time) of a 1 min sequence recorded at 6s frame interval. The membrane topography clearly reflects the underlying α-CD3 adhesive patches (Minimal Time Projection, Min). However, the cell membrane exhibits strong protrusion activity as seen in the Maximal Time Projection (Max) and Standard Deviation (SD). (B) ZAP-70-GFP cells establish contact with the substrate through puncta (blue circles) which preferentially target the zones with underlying patterned α-CD3. In these zones, Zap-70 is clustered after further spreading (maximal projection), but some of these clusters may eventually disappear.

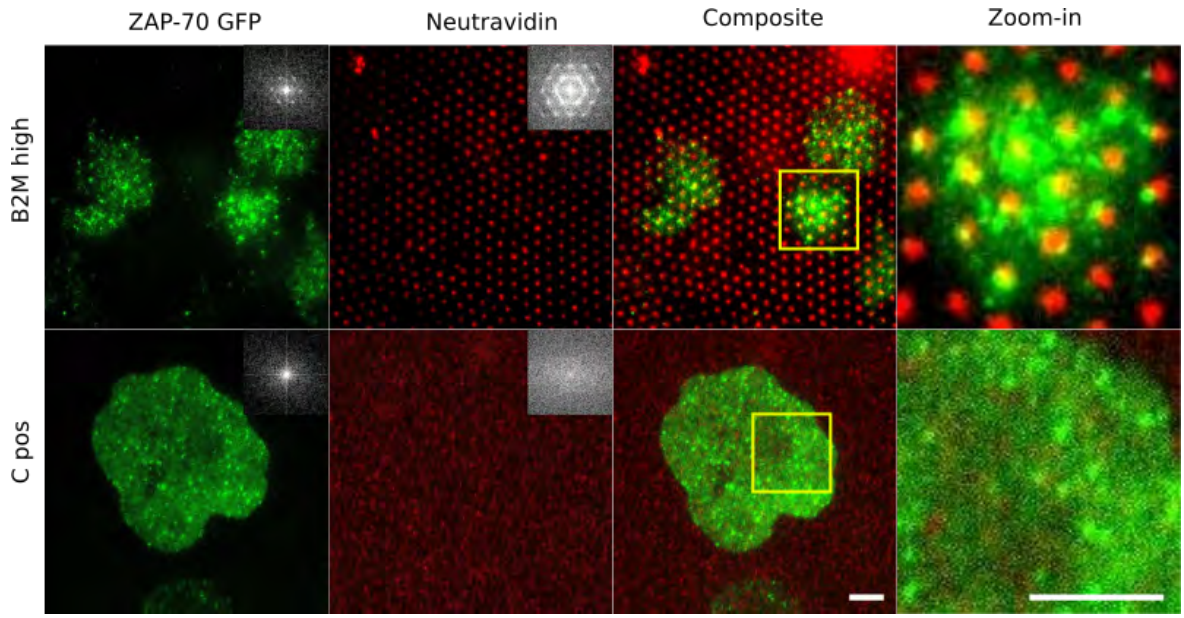

Fig. 6 Distribution of ZAP-70. Jurkat cells expressing ZAP-70-GFP were allowed to interact with B2M dots with high PEG density and were fixed before observation. The bottom row shows the corresponding positive control. Column 1: The ZAP-70 clusters are randomly distributed on the positive control but are partially ordered on the pattern. The corresponding FFTs in the inset confirm this. Column 2: the underlying fluorescent dots (or uniformly distributed NAV). Column 3: a superposition of the ZAP-70 channel and the NAV channel (Column 4: zoom-in) shows that the overlap is imperfect. Scale bar 3 μm.

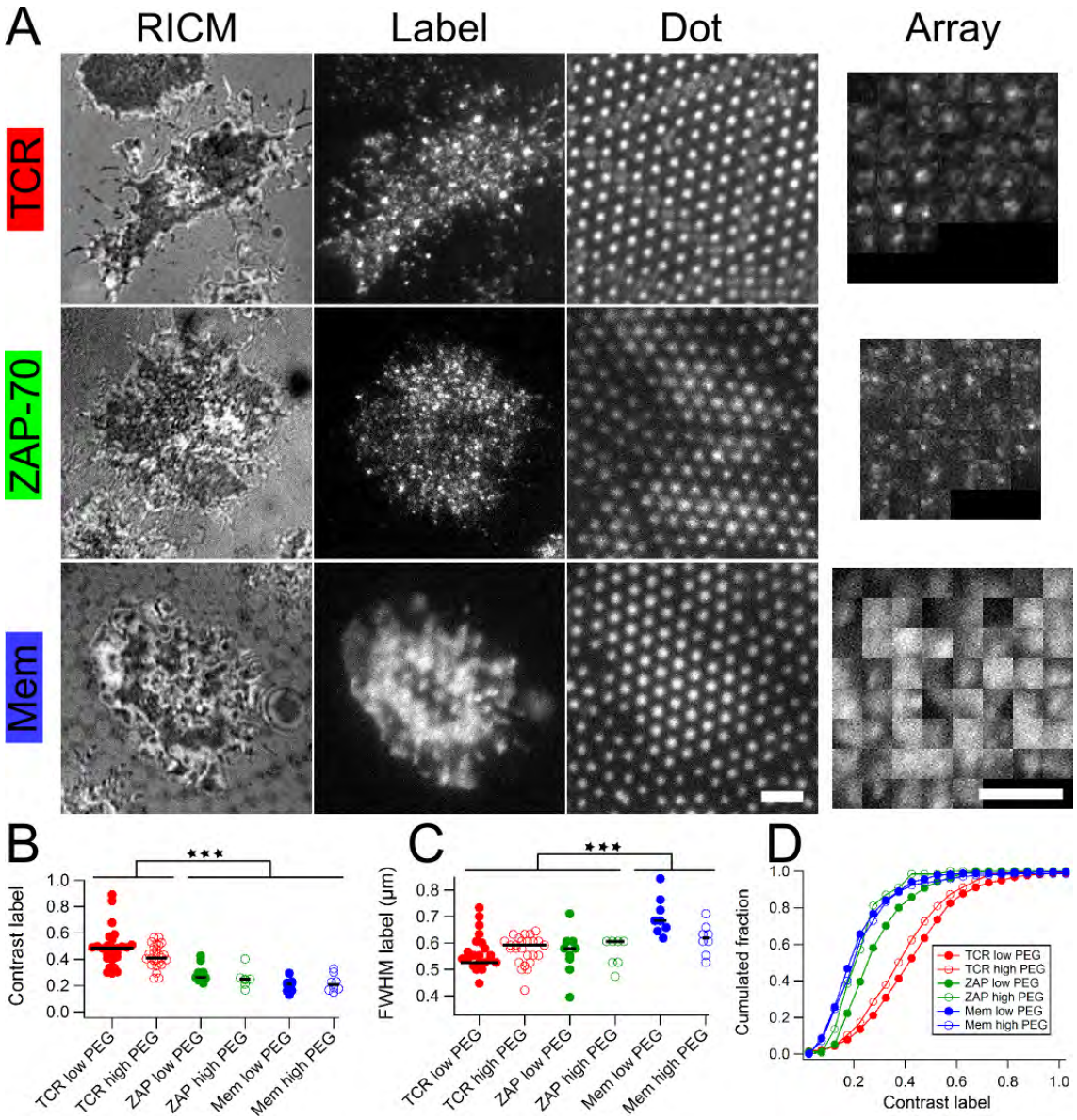

Fig. 7 Dot-scale analysis of the effect of patterned α-CD3 on TCR and ZAP-70 recruitment. Cells were engaged during 30 min on substrates patterned with α-CD3 dots (B2M low: pitch 2 μm and dot size 0.7μm with low PEG density between the dots or B2M high, same with high PEG density). (A) Cells on B2M low were fluorescently labeled for TCR, ZAP-70 or Membrane. In each case, a cell showing median values for the cluster size and contrast parameters was randomly chosen for illustration. From left to right, RICM, TIRFM image of the label and epi-fluorescence image of the dots are shown. The last column is an array representation of the label clusters and shows the fluorescence of the label in square regions centered on each underlying dot. Scale bar: 2μm. (B-C) Scatter dot plot of label contrast and full width at half maximum. Each dot represents the median value for all dots under one given cell. Black bar represents the median of the dots. *** : $P < 0.001$. (D) Cumulated fraction of contrast calculated on dots for all cells in a given condition.

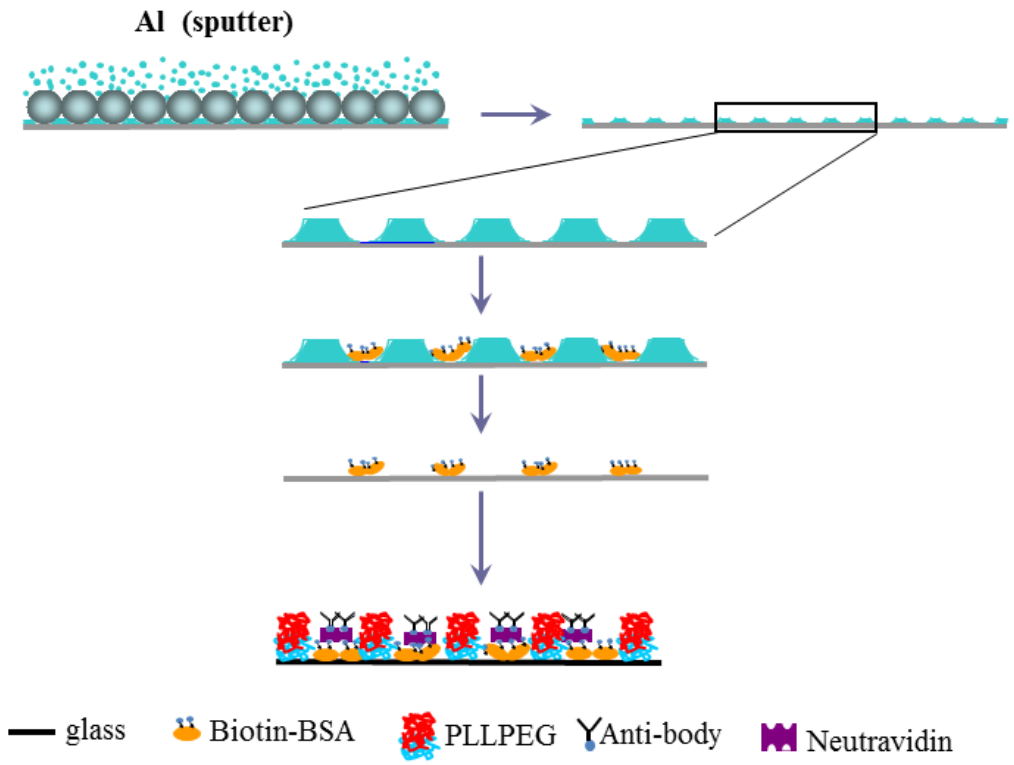

SI Figure 1. Schematic representation of the process of creating the size-tunable protein nano-dot arrays. Top row: a colloidal bead mask is used to sputter deposit aluminium upto a controlled thickness. Subsequent rows top to bottom: zoom in of the secondary aluminium mask, deposition of BSA-biotin as place holder, removal of aluminium by chemical lift-off, blocking of bare glass with PLL-PEG and functionalization of BSA-biotin. Note that the figure is not to scale. The diameter of the beads is of the order of micro-meters, the aluminium layer may be about 50 to several hundred nano-meters thick, and the size of the holes, which ultimately determine the size of the protein nano-dots, is variable between 300 nm and about 2 μm

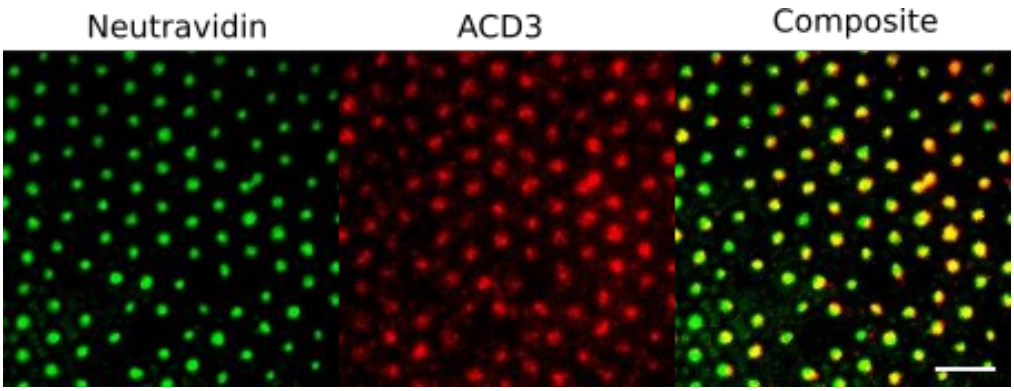

SI Figure 2. α-CD3 dots. Neutravidin dots were functionalized with fluorescent labelled α-CD3. The samples were imaged in epi-fluorescence in the Alexa 488 channel (Neutravidin) and the Atto 647 channel (α-CD3). The composite image show good correspondence between the two channels.

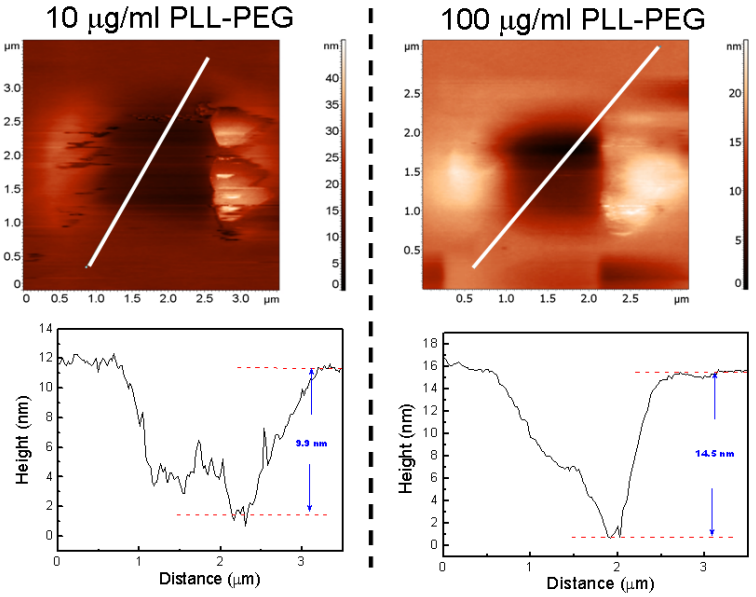

SI Figure 3. AFM image of PEG layer with scratched hole to measure layer thickness. Tapping mode AFM (NTEGRA system, NT-MDT, Russia) image (top) and the height profile corresponding to the white lines (bottom), for low (10 μg/ml PLL-PEG) and high (100 μg/ml PLL-PEG) PEG surface density. Silicon tips (CSC35, MikroMash, Bulgaria) with a typical resonance frequency of 110 kHz and a force constant 5.5 N/m were used to make holes in the homogeneous PEG layer on glass by scratching. The same (or equivalent) tips were used for imaging the hole in order to infer the layer thickness. Imaging was done at room temperature in PBS buffer (pH = 7.2). The PEG layer is thicker (about 14.5 nm) for the high PEG case as compared to the low PEG case (about 10 nm).

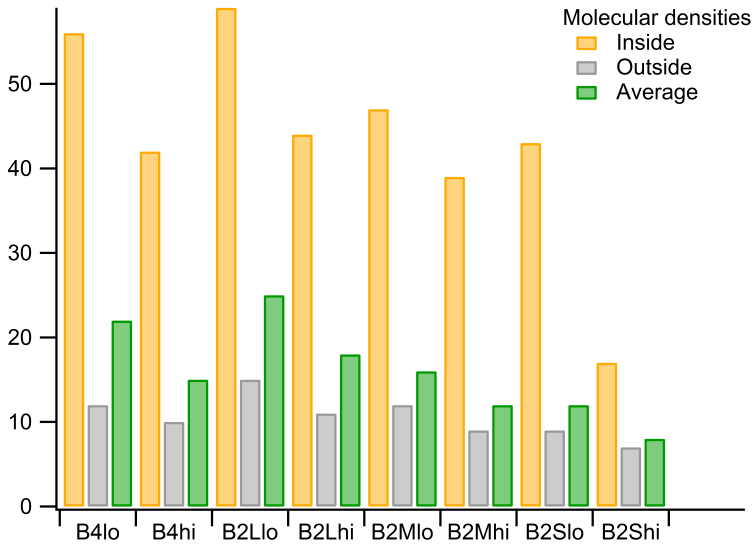

SI Figure 4. Molecular densities of neutravidin expressed as number/μm^2. The overall average, and averages inside the dot and outside the dot are reported. The overall average was measured directly from fluorescent intensity by considering a large area with many dots. The inside and outside densities could not be separately determined for the 500 nm pitch (300 nm dot size).

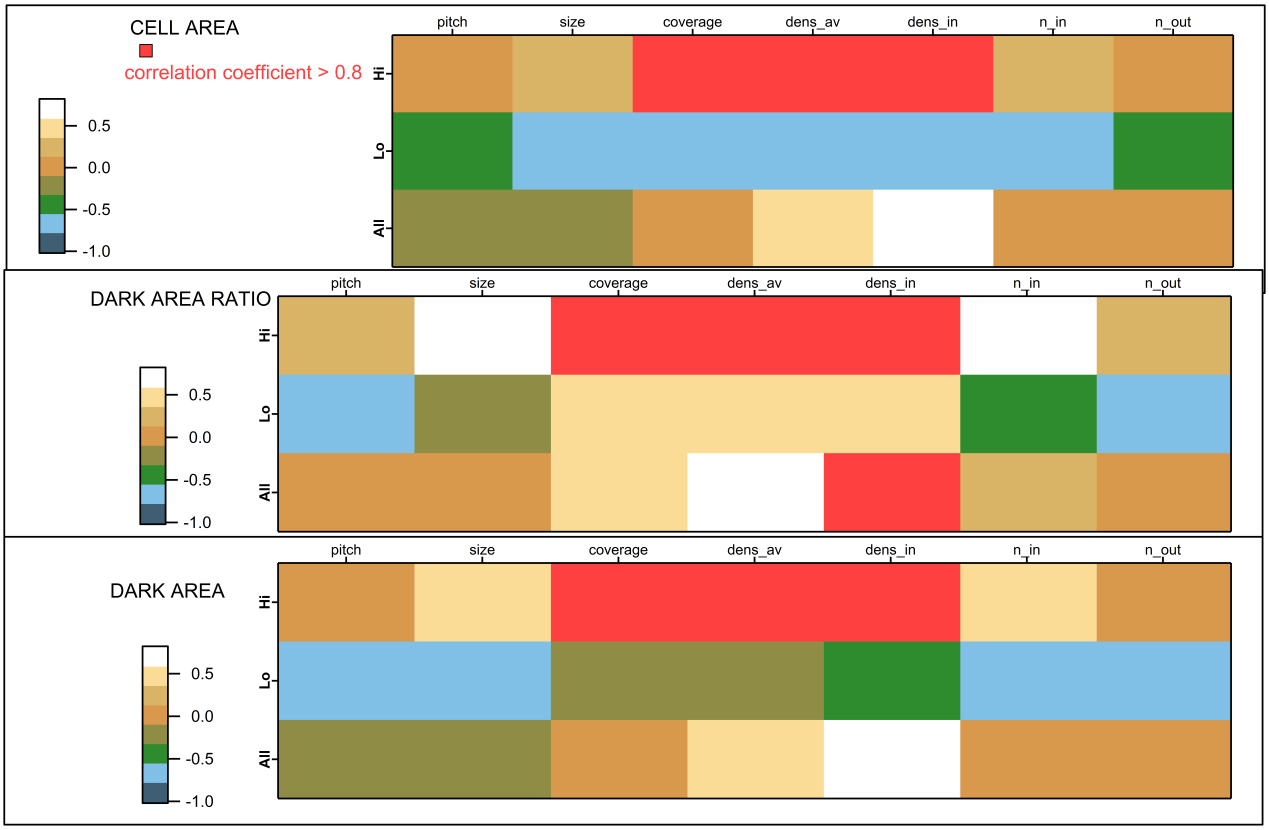

SI Figure 5. Pearson correlation coefficient for correlation between a readout-parameter (top panel: contact zone area "cell area", middle panel: ratio of tight adhesion area to contact area "dark area ratio", and bottom panel: absolute value of tight adhesion area "dark area"), and all possible dot-characteristics (rows: pitch, size, coverage, average molecular density "dens_av", inside density "dens_in", number inside dots "n_in", number outside dots "n_out"), for either high PEG (top row in each panel) or low PEG (middle row), or for the two taken together (bottom row). High correlations (> 0.6) are coloured red. For cell surface contact area, high correlations occur only for the case of high PEG surface density, and for the parameters - coverage, average density and density inside the dots. Since the average density depends both on the coverage and the density inside the dots, we take the average density as the relevant parameter to test further. For the ratio of tight adhesion to total area (dark area ratio), high correlations again occur for the case of high PEG surface density. Interestingly, considering high as well as low PEG density together (all), a strong correlation with density of ligands inside the dots is revealed. For the absolute value of tight adhesion area (dark area), the correlations are same as for contact area.

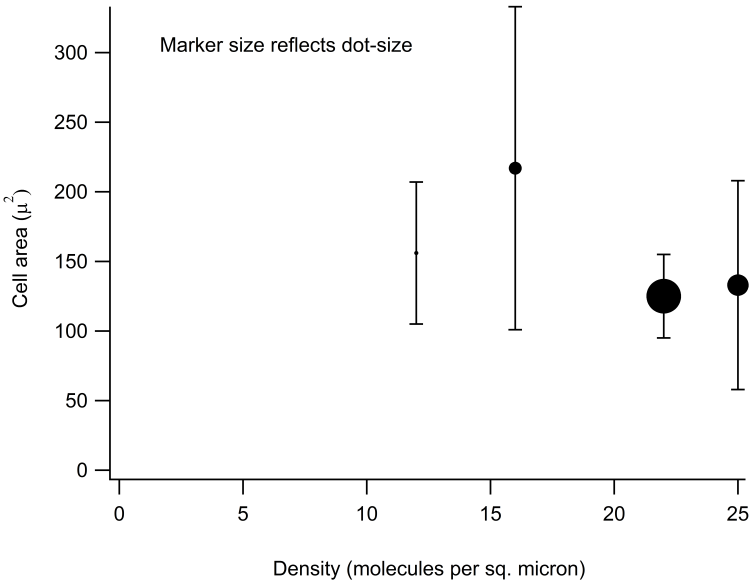

SI Figure 6. The contact zone area (cell area) as function of average ligand density for case of low surface density PEG layer.

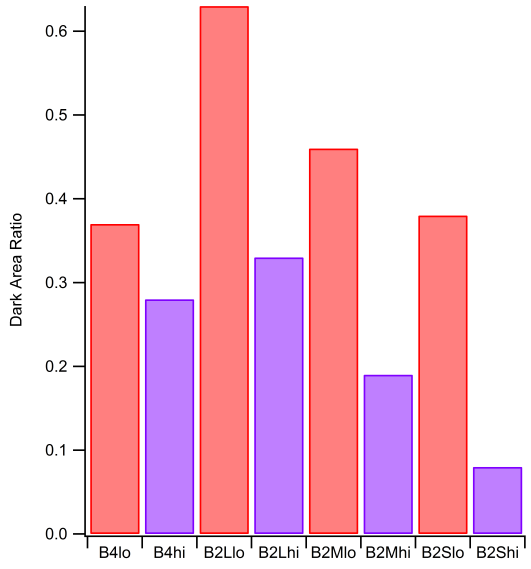

SI Figure 7. The ratio of the contact zone area and tight adhesion area as detected in RICM (dark area ratio). Red: low surface density PEG, Blue: high surface density PEG.

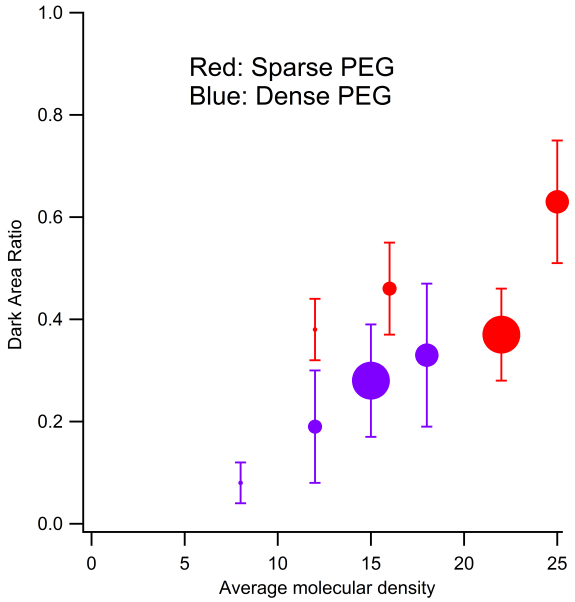

SI Figure 8. The ratio of the contact zone area and tight adhesion area as detected in RICM (dark area ratio) as function of average molecular density of the ligands. Molecular densities are expressed as number/μm^2. For high PEG case (blue, dense PEG), a strong correlation is discernible, but this is not the case for low PEG (red, sparse PEG).

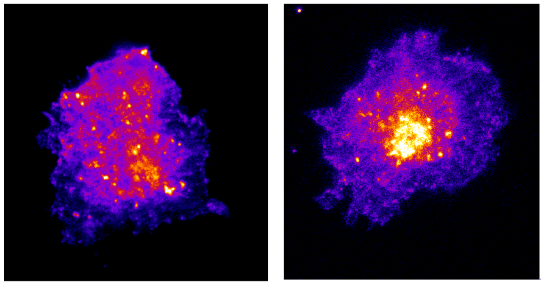

SI Figure 9. Formation of TCR micro-clusters on Pos. Live cells were labelled with anti-Vβ8 prior to spreading and were allowed to spread on c Pos substrates as described in the main text for wild type cells. The pre-labelling treatment "pre-activates" the cells resulting in clearly visible TCR microclusters (left), which may sometimes even coalesce into a cSMAC (right). Compare with Fig. 4A where the cells were labelled with anti-Vβ8 after fixation.

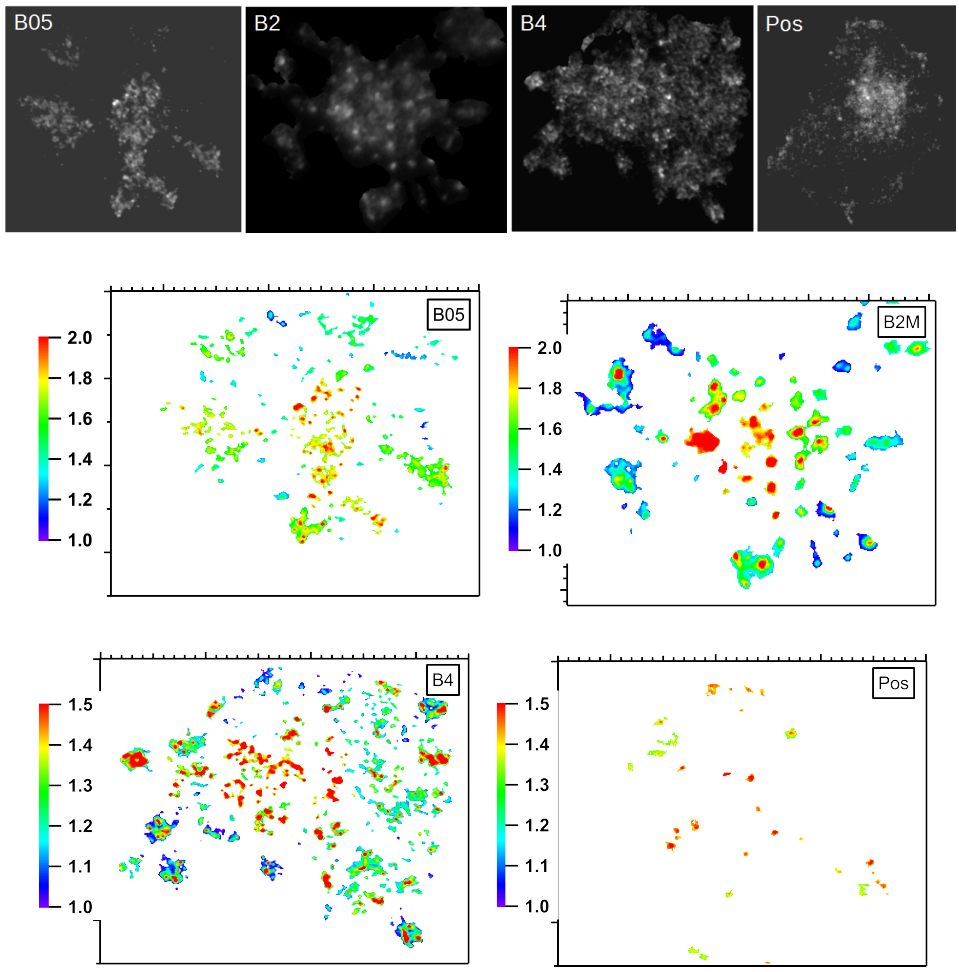

SI Figure 10. Analysis of TCR clusters. Top: TIRF-M images of fixed cells with labeled TCR on different substrate types. Bottom: corresponding images of clusters segmented using the analysis algorithm described in the main text. Each image is 28μmX28μm. In each image, the intensity was normalized by the average intensity under the cell, and thus the colour is a direct representation of the enrichment of TCR in a cluster. Note that the colour scale is slightly different for each image and was chosen to highlight the heterogeneity in TCR concentration within the larger clusters.

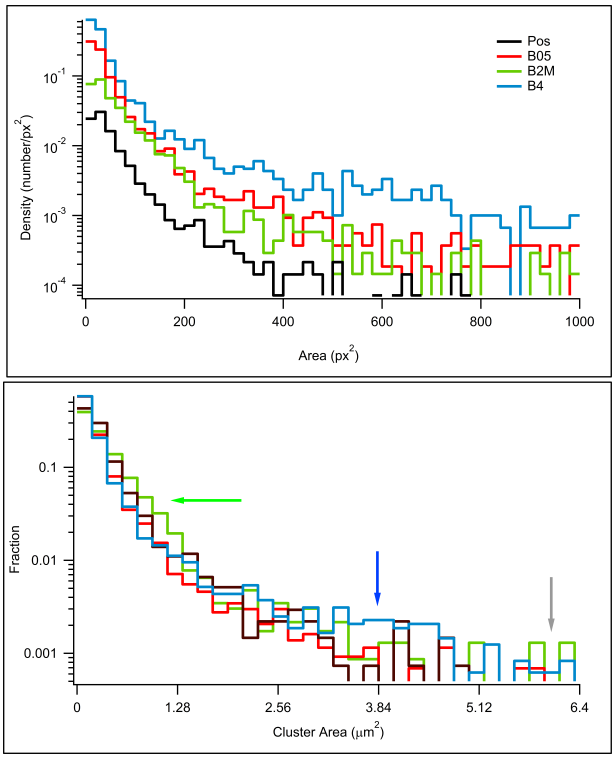

SI Figure 11. Histograms of TCR-cluster size distribution normalized either by cell size (top) or by total number of detected clusters (bottom, corresponds to Figure 4C in main text, see main text for explanation of arrows).

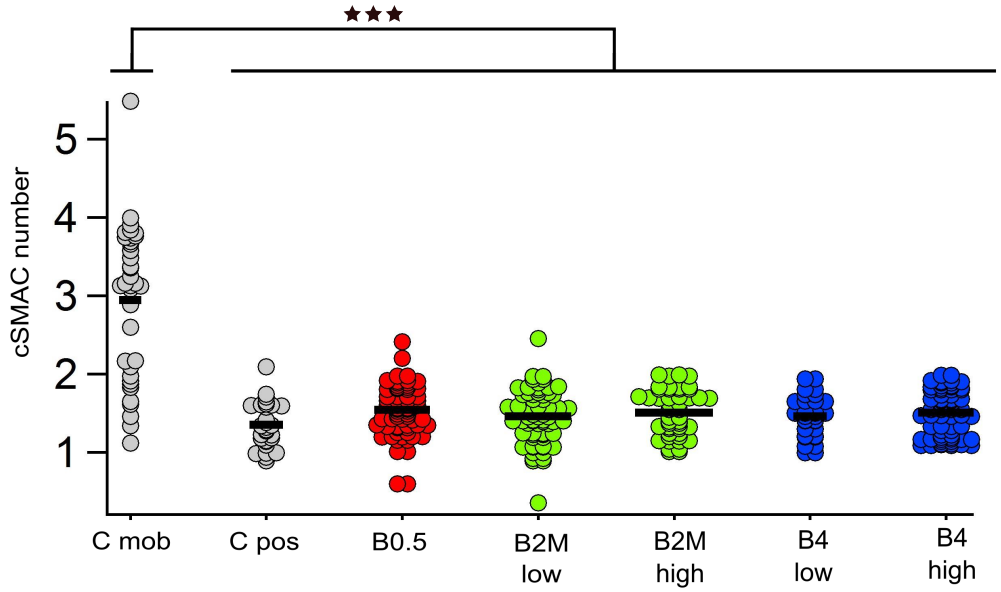

SI Figure 12. Quantification of the degree of centralization of labeled TCR using a cSMAC number, and comparison with positive controls with immobilized or mobile ligands. The cSMAC number corresponds to the ratio between the fluorescence signal measured in a 2 μm radius circle at the center of the contact zone (as determined by RICM) and the fluorescence signal of the rest of the contact zone (Dillard et al. 2014). This measure evaluates the formation of the immune synapse by quantifying the gathering of the TCR molecules. On this graph, we can see that neither the patterned substrates nor the substrates presenting fixed ligands (C pos) show TCR gathering at the center (cSMAC number ≈ 1). On substrates with mobile ligands (c mob), as expected, gathering is present (cSMAC number $>> 1$).

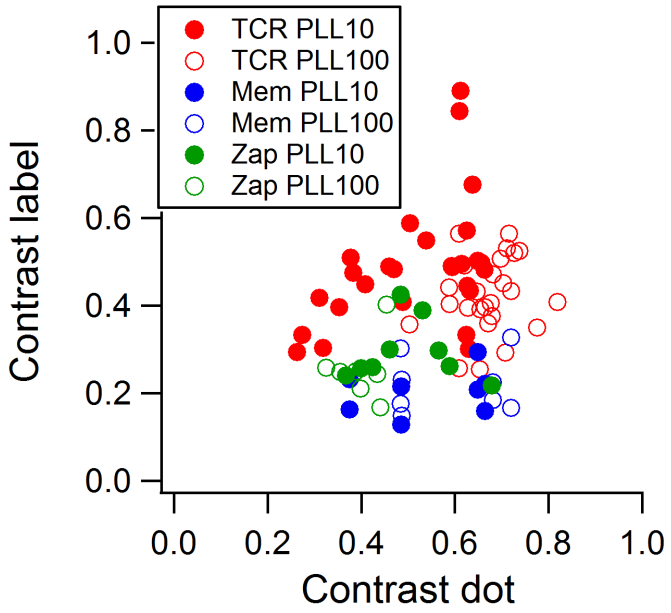

SI Figure 13. Dot contrast and label contrast are not correlated. The contrast between the inside and outside of NAV-dots was determined for the neutravidin channel and the label on the cell, on a dot-by-dot basis. Each symbol on the graph represents the median dot contrast taken over a single cell. Plotting them against each other does not show any correlation. The different labels are plotted in different colors as shown in the legend. Open circles correspond to high PEG density (PLL 100) and closed circles to low PEG density (PLL 10).

Table 1. Characteristics of the positive and negative controls.

Acronym	Description of NAV and α-CD3	Description of PLL-PEG	Comments
c Pos	Homogeneous	No exposure	
c Pos high		Exposure:high concentration*	Some α-CD3 may be "hidden" by PEG.
c Pos low		Exposure:low concentration*	No effect on the cell area†, small effect on roughness‡
c Neg high	Exposure$^{\circ}$	Grafted at high concentration	Extra α-CD3 may be available for binding to TCR
c Neg low		Grafted at low concentration	Accounted for in measured average ligand density

* Exposure to high/low concentration PLL-PEG solution at the BSA-biotin stage. † Data not shown. ‡ Main text Fig. 4. $^{\circ}$ Exposure to protein solutions after PEG grafting